Published in final edited form as:

Arterioscler Thromb Vasc Biol. 2024 February ; 44(2): 366–390. doi:10.1161/ATVBAHA.123.320279.

Requirement of site-specific tyrosine phosphorylation of cortactin in retinal neovascularization and vascular leakage

Raj Kumar[1], **Klemens Rottner**[2,3], **Gadiparthi N. Rao**[1]

[1]Department of Physiology, University of Tennessee Health Science Center, Memphis, TN 38163, USA

[2]Division of Molecular Cell Biology, Zoological Institute, Technische Universität Braunschweig, Spielmannstrasse 7, 38106 Braunschweig, Germany

[3]Department of Cell Biology, Helmholtz Centre for Infection Research, Inhoffenstrasse 7, 38124 Braunschweig, Germany

Abstract

BACKGROUND: Retinal neovascularization is a major cause of vision impairment. Therefore, the purpose of this study is to investigate the mechanisms by which hypoxia triggers the development of abnormal and leaky blood vessels.

METHODS: A variety of cellular and molecular approaches as well as tissue-specific knockout mice were used to investigate the role of cortactin in retinal neovascularization and vascular leakage.

RESULTS: We found that VEGFA stimulates cortactin phosphorylation at Y421, Y453, and Y470 residues in human retinal microvascular endothelial cells (HRMVECs). In addition, we observed that while blockade of cortactin phosphorylation at Y470 inhibited VEGFA-induced HRMVEC angiogenic events, suppression of Y421 phosphorylation protected endothelial barrier integrity from disruption by VEGFA. In line with these observations, while blockade of cortactin phosphorylation at Y470 negated OIR-induced retinal neovascularization, interference with Y421 phosphorylation prevented VEGFA/OIR-induced vascular leakage. Mechanistically, while phosphorylation at Y470 was required for its interaction with Arp2/3 and CDC6 facilitating actin polymerization and DNA synthesis, respectively, cortactin phosphorylation at Y421 leads to its dissociation from VE-cadherin, resulting in adherens junction disruption. Furthermore, whereas cortactin phosphorylation at Y470 residue was dependent on Lyn, its phosphorylation at Y421 residue required Syk activation. Accordingly, lentivirus-mediated expression of shRNA targeting Lyn or Syk levels inhibited OIR-induced retinal neovascularization and vascular leakage, respectively.

CONCLUSIONS: The above observations show for the first time that phosphorylation of cortactin is involved in a site-specific manner in the regulation of retinal neovascularization and

Address correspondence to: Gadiparthi N. Rao, Ph.D., Department of Physiology, 71 S Manassas Street, TSRB, Room 310J, University of Tennessee Health Science Center, Memphis, TN 38163, USA, rgadipar@uthsc.edu.

Disclosures: None

vascular leakage. In view of these findings, cortactin could be a novel target for the development of therapeutics against vascular diseases such as retinal neovascularization and vascular leakage.

Graphical Abstract

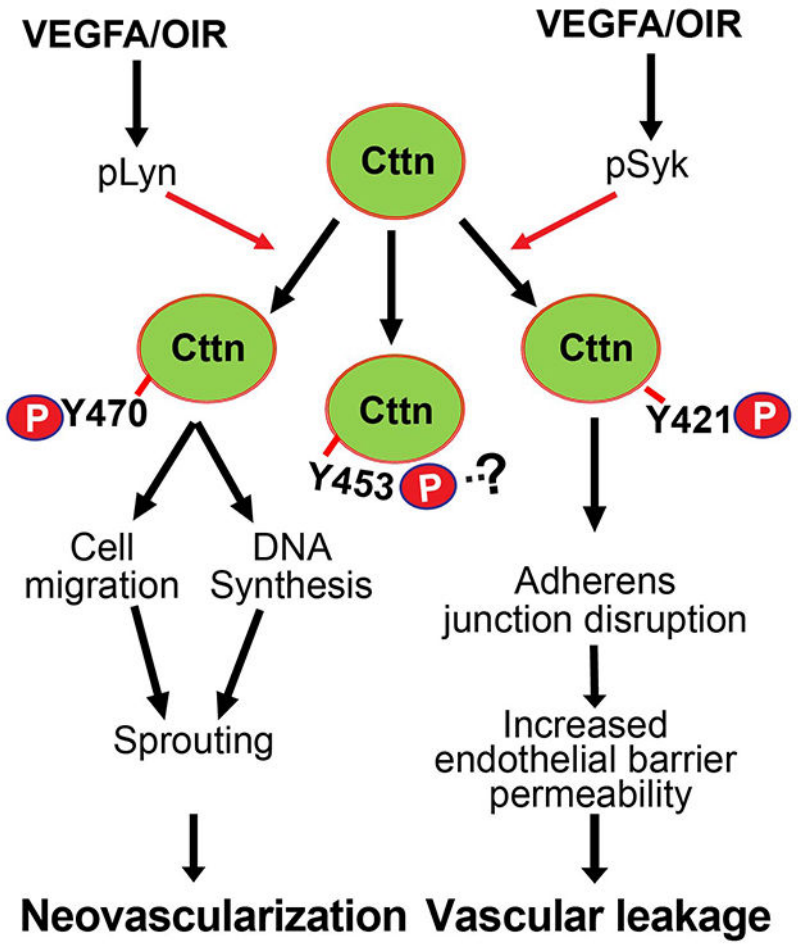

Keywords

Cortactin; endothelial cells; neovascularization; vascular leakage; vascular endothelial growth factor

INTRODUCTION

Diabetic retinopathy (DR) is a leading cause of visual impairment and vision loss worldwide (1, 2). Epidemiology data indicates that among the 34.4 million US adults with diagnosed diabetes, almost 12% of these individuals were reported with vision disability (3). In addition, the number of people with diagnosed diabetes is predicted to rise to 63 million by 2045 in the USA, which is an alarming factor for an increased incidence of DR (4). Based on the progression of microvascular lesions and changes in the nonvascular cell types in the lesions, DR is classified into an early stage of “non-proliferative diabetic retinopathy”

(NPDR) and advanced stage of “proliferative diabetic retinopathy” (PDR) (5). NPDR is characterized by microaneurysms and blockage of blood vessels, which restricts blood supply to the retinal tissue resulting in the development of hypoxia (6). The hypoxic tissue then stimulates the secretion of several growth factors, including vascular endothelial growth factor (VEGF), which influence the development of new blood vessels in that area (7). On the other hand, PDR is an advanced stage of NPDR where newly developed blood vessels grow along the inner surface of the retina into the vitreous (8). Thus, PDR is characterized by retinal neovascularization comprising fragile and leaky blood vessels that leads to the development of a scar retina that in a later stage can result in the retinal detachment from the underlying sclera (8). Furthermore, the leaky blood vessels allow the passage of circulating cells and proteins into the neural retina (9). Together, all these changes could damage retinal neurons and contribute to vision loss (10). It appears that VEGF produced by hypoxic retina triggers the development of nonproductive pathological angiogenesis instead of reparative angiogenesis (11, 12). Accordingly, many multicenter randomized clinical trials have been focused on anti-VEGF therapies in treating retinal neovascularization in DR patients (13). However, anti-VEGF therapy was found to be effective in some, but not all patients (14, 15).

The formation of new blood vessels through vasculogenesis and further expansion of the network by angiogenesis appears to be dependent on coordinated EC migration, proliferation and sprouting, which are critically dependent on cytoskeleton remodeling (16). Actin, which is one of the most abundant intracellular cytoskeletal proteins in mammalian cells, through its reorganization plays an important role in the regulation of cell shape, cell migration, cell division, and transcriptional responses (17). As total actin content per cell was not affected during these events, they are achieved by modulation of the ratio of **f**ilamentous (F-)actin to monomeric, also called **g**lobular (G-)actin (18, 19). The helical F-actin filaments are continuously produced in the cytoskeleton by incorporating Mg^{2+}/ATP-bound G-actin monomers into the growing filaments at their fast-growing, so-called barbed ends (20). The resulting F-actin cytoskeleton organized in structures such as lamellipodia, filopodia, or stress fibers mediates various cellular functions (17). However, F-actin cytoskeleton remodeling is dynamically regulated by actin interactions with a plethora of actin-binding proteins (21). The actin-binding proteins can cross-link actin filaments and thus stabilize or enforce given cytoskeletal structures or modulate their interactions with other cytoskeletal components and regulators (22). Cortactin is one member of a family of F-actin-binding proteins playing important roles in cellular functions (23, 24). Mechanistically, cortactin can bind both actin filaments and one of its prominent nucleators, the actin-related protein 2/3 (Arp2/3) complex, and is thereby thought to stabilize actin filament branches formed by this prominent complex (25, 26). Aside from this, many reports indicate that cortactin constitutes a key player in aggressive cancers (27). Cortactin was found overexpressed in breast cancer (28), colorectal cancer (29), gliosarcoma (30), lung squamous cell carcinoma (31), melanoma (32), and neck squamous cell carcinoma (33). In carcinoma, cortactin was not only observed to be overexpressed, but also to undergo posttranslational modifications, such as phosphorylation thereby mediating enhanced cancer cell migration (34, 35). In addition, deacetylation of cortactin by HDAC6 was described to be linked to endothelial cell migration and angiogenesis (36). Thus, cortactin function appears to be dependent on its induction of expression as well as post-translational modifications.

However, the role of cortactin and its posttranslational modifications in pathological angiogenesis such as retinal neovascularization is unknown. To this end, our results show for the first time that VEGFA phosphorylates cortactin at tyrosine residues 421, 453, and 470 in human retinal microvascular endothelial cells (HRMVECs). Furthermore, while cortactin phosphorylation at Y470 was required for retinal neovascularization, phosphorylation at Y421 was involved in vascular leakage. Besides that, while cortactin phosphorylation at Y470 requires Lyn activation, its phosphorylation at Y421 was dependent on Syk activation in mediating retinal neovascularization and vascular leakage, respectively.

MATERIALS AND METHODS

The data that support the findings of this study are available from the corresponding author upon reasonable request.

Reagents

Recombinant human VEGF165a (Cat No. 293-VE-010/CF) and Mouse VEGFA 164a (Cat No. 493-MV-025/CF) were bought from R&D Systems (Minneapolis, MN). Growth factor-reduced Matrigel (Cat No. 354230) was purchased from BD Biosciences (Bedford, MA). Anti-Btk (sc-1696), anti-CDC6 (sc-9964), anti-Cortactin (sc-55579), anti-Fak (sc-1688), anti-Frk (sc-166478), anti-Fyn (sc-365913), anti-Lyn (sc-7274), anti-MEK1 (sc-6250), anti-p53 (sc-126), anti-Syk (sc-573), anti-Yes (sc-8403) and anti-β-Tubulin (sc-5274) antibodies were obtained from Santa Cruz Biotechnology (Santa Cruz, CA). Mouse anti-CD31 antibody (Cat No. 550274) was bought from BD Pharmingen (Palo Alto, CA). Anti-pFyn (Y530) (ab192172), anti-Ki67 (ab15580), anti-pLyn (Y507) (ab33914), and anti-Pyk2 (ab32571) antibodies were obtained from Abcam (Cambridge, MA). Anti-Src (Cat No. 05-184) and anti-pTyr antibody (PY20) (Cat No. 05-777) were purchased from EMD Millipore (Burlington, MA). [^{3}H]-Thymidine (Cat No. NET027E001MC, s.a. 20 Ci/mmole) was bought from Perkin Elmer (Boston, MA). Syk inhibitor (BAY61-3606) (Cat No. ALX-270-479) was obtained from Enzo Life Sciences (Farmingdale, NY). Endothelial basal medium (EBM) (CC-3133), and endothelial growth medium (EGM) SingleQuot kit supplements and growth factors (CC-4133) were bought from Lonza (Walkersville, MD). Cytodex microcarrier beads (Cat No. C3278) and thrombin (Cat No. T8885) were obtained from Sigma Aldrich (St Louis, MO). Fibrinogen (Cat No. 820224) was procured from MP Biomedicals LCC (Solon, OH). Anti-Arp2 (Cat No. 3128), anti-Arp3 (Cat No. 4738), anti-pBtk (Y223) (Cat No. 5082), anti-pFak (Y397) (Cat No. 3291), anti-pPyk2 (Y402) (Cat No. 3291), anti-pSrc (Y416) (Cat No. 2101) and anti-pSyk (Y323) (Cat No. 2715) were obtained from Cell Signaling Technology (Danvers, MA). Anti-pCortactin (Y421) (Cat No. 44-854G), anti-pCortactin (Y466/Y470) (Cat No. 44-856), and anti-pYes (Y537) (Cat No. PA5-12698) antibodies, human Lyn siRNA (Id: s8358), human Rac1 siRNA (Id: s11711), human RhoA siRNA (Id: s759), human Src siRNA (Id: s13411), Invivofectamine 3.0 (Cat No. IVF3001), Nuclear and cytoplasmic extraction kit (Cat No. 78835), Phalloidin (Cat No. A12380), and lipofectamine 3000 transfection reagent (Cat No. L-3000-015) were purchased from Thermo Fisher Scientific (Waltham, MA). Arp2/3 inhibitor (CK666) (Cat No. 3950), Evans blue (Cat No. 0845), and Pyk2 inhibitor (PF431396) (Cat No. 4278) were obtained from Tocris Bioscience (Minneapolis, MN). Cell tracker green (C7025),

goat anti-rabbit IgG-AlexaFluor 488 (A11034), goat anti-rat IgG-AlexaFluor 568 (A11077), goat anti-rat IgG-AlexaFluor 350 (A21093), Hoechst 3342, isolectin B4-594 (I21413) and Prolong Gold antifade reagent (P36930) were bought from Molecular Probes (Eugene, OR).

Plasmids

Cloning of human cortactin Y421F, Y446F, Y453F, Y470F, and Y486F mutant plasmids were described previously (37).

Lentiviral shRNA particles

Non-mammalian non-target control (Cat No. SHC0002V), Lyn (Cat No. SHCLNV; Clone ID #TRCN0000023664), and Syk (Cat No. SHCLNV; Clone ID #TRCN0000023569) MISSON shRNA lentiviral particles were obtained from Sigma Aldrich (St Louis, MO). For transduction into retina, 10^6 viral particles were intravitreally injected once into mouse pups at P10.

Mice

C57BL/6J (WT) (strain code 027) pregnant mice at E16 were bought from Charles River Laboratories (Wilmington, MA). Cdh5-Cre^{ERT2} mice were obtained from Dr. Luisa Iruela-Arispe at the University of California in Los Angeles, CA. Generation of Cortactin$^{flox/flox}$ mice was described previously (38). To delete cortactin in endothelium during postnatal development, we crossbred Cortactin$^{flox/flox}$ mice with Cdh5-Cre^{ERT2} mice to generate cortactin$^{flox/-}$:Cdh5-Cre^{ERT2} mice. These mice were then backcrossed with Cortactin$^{flox/flox}$ mice to generate Cortactin$^{flox/flox}$:Cdh5-Cre^{ERT2} litters. To induce Cre activity, 2 consecutive intraperitoneal injections of tamoxifen (50 μl) (Sigma-Aldrich, T5648; 2 mg/ml in 10% ethanol and 90% corn oil) were given to mice pups at P9 and P10 to delete cortactin in the endothelium (Cortactin$^{i\Delta EC}$). Tamoxifen was also injected into Cortactin$^{flox/flox}$ mice pups as a control. The mice strains used in this study were free of RD1 and RD8 mutations (39, 40), as revealed by genotyping (Figure S1). Mice were fed with Tekland irradiated LM-485 diet (Cat # 7912), bred, and maintained at the University of Tennessee Health Science Center's vivarium. All experiments involving animals were approved by the Institutional Animal Care and Use Committee (IACUC) of the University of Tennessee Health Science Center (Memphis, TN).

Cell culture

Human retinal microvascular endothelial cells (HRMVECs; Cat No. ACBRI 181) were purchased from Cell Systems (Kirkland, WA) and grown in EGM containing growth supplements, 10 μg/ml gentamycin, and 0.25 μg/ml amphotericin B. Human fibroblasts (Cat No. PCS-201-013) were obtained from American Type Culture Collection (Manassas, VA) and grown in EGM containing growth supplements, 10 μg/ml gentamycin, and 0.25 μg/m amphotericin B. Cultures were maintained at 37°C in a humidified 95% air and 5% CO_2 atmosphere. HRMVECs with passage numbers between 5 and 10 were synchronized by maintaining cells in growth factor-free EBM for 24 h and were used to perform the experiments unless otherwise indicated.

Cell migration

HRMVEC migration was measured by wound-healing assays essentially as described previously (41). Briefly, HRMVECs were plated at 2 x 10^5 cells/ml in each chamber of the ibidi culture inserts and grown to full confluency. Following a 24-h growth arrest period in EBM, the inserts were removed using sterile tweezers, and 1 ml of EBM containing 5 mM hydroxyurea was added. Cells were treated with and without VEGFA (40 ng/ml) for 24 h at which time the migrated cells were observed under a Nikon Eclipse TS100 microscope with a 4X/0.13 NA objective, and the images were captured with a Nikon Digital Sight DS-L1 camera. Cell migration was expressed as percentage of wound closure (total area minus area not occupied by the cells/total area × 100). Wherever plasmids were used, cells were transfected with either pCMV empty vector or expression vector for the indicated gene and then allowed to grow to 70% to 80% confluence. Cells were then trypsinized, plated at 2 × 10^5 cells/ml in each chamber of the ibidi culture inserts, and subjected to migration assay.

DNA synthesis

DNA synthesis was measured by [^{3}H]-thymidine incorporation as described previously (42). Briefly, cells were transfected with either pCMV or pCMV-Cttn plasmids. Cells were then plated onto 6-well plates, allowed to grow to 70% to 80% confluence, synchronized for 24 h, and then treated with or without VEGFA (40 ng/ml) for 24 h. After 6 h of VEGFA addition, cells were pulse-labeled with 1 μCi/ml of [^{3}H]-thymidine for 18 h. After a 24-h incubation period, cells were washed with cold PBS, trypsinized, and pelleted by centrifugation. The cell pellet was resuspended in 3 ml of 20% (w/v) cold TCA and vortexed vigorously to lyse cells. The mixture was then kept on ice for 30 minutes and passed through a GF/F glass microfiber filter. The filter was washed first with 3 ml of 5% cold TCA and then 3 ml of cold ethanol, then dried, placed in a liquid scintillation vial containing 5 ml of scintillation fluid, and the radioactivity counted in a liquid scintillation counter (Beckman LS 3801). DNA synthesis was expressed as fold changes in cpm per dish over control.

Lamellipodia formation

Lamellipodia formation was measured as described previously (43). Cells were transfected with either pCMV or pCMV-Cttn (Y470F) expression plasmids, trypsinized, pelleted and seeded onto coverslips in 6-well plates. At 70% to 80% confluency, cells were synchronized for 24 h and treated with or without VEGFA (40 ng/mL) for 2 h. Cells were then washed with cold PBS, fixed in 4% paraformaldehyde, permeabilized with 0.3% Triton X100, blocked with 3% BSA and incubated with anti-Arp3 antibody (1:100) overnight followed by incubation with Alexa Fluor 488-conjugated goat anti-rabbit secondary antibody and Alexa Fluor 568 Phalloidin. Cells were observed under a Zeiss inverted microscope (Axiovision Observer.z1; 40X/NA 0.6), and the fluorescence images were captured by a Zeiss AxioCam MRm camera using the microscope operating and image analysis software Zen 2.6 (blue edition) (Carl Zeiss Imaging Solutions GmbH). Lamellipodia were identified by visualizing F-actin/Arp3 colocalization at the edges of each cell.

Three-dimensional sprouting assay

A three-dimensional sprouting assay was performed as described previously (42). Briefly, cells were transfected with either pCMV or pCMV-Cttn plasmids. Cells were labeled with a cell tracker, trypsinized, pelleted, and then, an equal number of cells was coated onto Cytodex beads for 6 h. Nonbinding cells were washed with PBS, and the beads embedded in fibrin gel. Human fibroblasts suspended in EGM with and without VEGFA (40 ng/ml) were seeded onto the top of the fibrin gel at a concentration of 2×10^4 cells/well and incubated at 37°C for 6 h, at which time the medium was replaced with fresh EGM with and without VEGFA, and incubation continued for 3 days. Sprouting was examined on day 3 under a Zeiss inverted fluorescence microscope (AxioVision Observer.z1; 10X/NA 0.45), and the fluorescence images were captured using a Zeiss AxioCam MRm camera, with microscope and camera operated by image analysis software Zen 2.6 (blue edition) (Carl Zeiss Imaging Solutions GmbH) (https://www.zeiss.com/content/dam/Microscopy/Downloads/Pdf/zenreleasenotes/zen-2_6_blue_edition-release-notes.pdf). Sprouting was expressed as the number of sprouts per bead.

Tube formation assay

Tube formation was measured as described previously (42). Briefly, cells were transfected with either pCMV or pCMV-Cttn plasmids. Cells were synchronized for 24 h and plated in a 24-well culture plate coated with growth factor-reduced Matrigel. Cells were added with or without VEGFA (40 ng/ml) and incubation continued for 6 h at 37°C. Tube formation was observed under an inverted phase contrast microscope (Eclipse TS100; Nikon, Tokyo, Japan), and the images were captured with a CCD color camera (KP-D20AU; Hitachi, Ibaraki, Japan) using Apple iMovie 7.1.4 software. The tube length was calculated using NIH ImageJ version 1.53 software (http://imagej.nih.gov/ij) and expressed in micrometers.

Stress fiber (F-actin) formation

Stress fiber formation was measured as described previously (44). Cells were transfected with either pCMV or pCMV-Cttn plasmids, plated on coverslips placed into 6-well plates, allowed to grow to 70% to 80% confluence, synchronized for 24 h, and then treated with or without VEGFA (40 ng/ml) for 2 h. After the incubation period, cells were washed with cold PBS, fixed in 4% paraformaldehyde, permeabilized with 0.3% Triton X100, and blocked with 3% BSA. Cells were then incubated with Alexa Fluor 568 Phalloidin (1:500) for 2 h, washed, counter stained with DAPI and mounted onto slides. The cells were then observed under a Zeiss inverted microscope (Axiovision Observer.z1; 40×/NA 0.6 or 10×/NA 0.45), and the fluorescence images captured by a Zeiss AxioCam MRm camera using the microscope operating and image analysis software Zen 2.6 (blue edition). Stress fibers were quantified by measuring the intensity of F-actin using ImageJ version 1.53 software and expressed as fold changes over control.

FITC-dextran flux assay

HRMVECs were grown to a confluent monolayer on the apical side of a 12-well trans-well (polycarbonate membrane with 0.4 μm pore size). The cells were growth-arrested for 6 h in EBM. The monolayer was treated with and without VEGFA (40 ng/ml) for

the indicated time periods. Wherever plasmids were used, cells were transfected with the indicated plasmid and 36 h later, these cells were seeded onto the trans-well. Fluorescein isothiocyanate-conjugated dextran (MW ~70 kDa) was added to the top chamber (apical surface) at 100 μg/ml concentration and incubated at 37°C for 2 h. The fluorescence intensity of the medium from each chamber (both apical and basal) was measured using SpectraMax Gemini XPS Spectrofluorometer (Molecular Devices). The permeability coefficient (Po) of dextran flux was calculated by using the following equation: Po (flux/hr/cm^2) = [(F1/ΔT) × VA]/(FA × A), where F1 is basal fluorescence; FA is apical fluorescence; ΔT, is change in time (hr); A is surface area (1.22 cm^2); VA is the volume of the medium in the basal chamber. The flux was expressed as % dextran flux/hr/cm^2 (45).

Trans-endothelial electrical resistance (TER)

HRMVECs were seeded onto the apical chamber of a 12-well trans-well (polycarbonate membrane with 0.4 μm pore size) at a density of 10^5 cells/cm^2. The cells were allowed to grow to a confluent monolayer and then growth-arrested for 6 h in EBM. The cells were treated with and without VEGFA (40 ng/ml) for the indicated time periods. Wherever plasmid was used, cells were transfected with the indicated plasmid, and 36 h later, these cells were seeded onto a trans-well. Resistance, as an index of barrier function, to current flow between cells and beneath the cell layer, created by cell-cell and cell-matrix components, was measured at various time periods using a Millicell ERS-2V-Ohm Meter (MERS00002, EMD Millipore). Trans-endothelial resistance was calculated using the following equation: TER = ($R_{sample} - R_{blank}$) × surface area of the trans-well. The surface area of 12-mm inserts, which were used in this study, is approximately 1.33 cm^2. Resistance was expressed as Ω.cm^2 (45).

Actin polymerization assay

Actin assembly was measured by using the pyrene-actin polymerization kit (BK003, Cytoskeleton, Inc.) following the manufacturer's instructions. Briefly, cells were transfected with pCMV-Cttn (WT) or pCMV-Cttn (mutant) plasmids and 36 h later, cells were growth-arrested in EGM and treated VEGFA for 30 minutes. Cell extracts were prepared, immunoprecipitated with anti-cortactin antibody, followed by incubation with Sepharose A beads (40 μl of 50 mg/ml slur), and the immunocomplexes eluted from the beads with 0.2 M glycine (pH 2.6) and neutralized by addition of an equal volume of 20 mM Tris-HCl (pH 8.5). To measure actin polymerization, stock pyrene-actin was diluted to 2.3 μM with actin buffer (5 mM Tris-HCl, pH 8.0, and 0.2 mM $CaCl_2$) containing 0.2 mM ATP and 0.5 mM DTT and stored on ice for 60 min to depolymerize the actin oligomers. The actin monomers were then collected by centrifugation at 18,800g for 30 minutes at 4°C. The pyrene-actin monomers were mixed with the eluted cortactin in a 96-well plate containing polymerization buffer (25 mM KCl and 1 mM $MgCl_2$, pH 7.0). The kinetics of actin polymerization were measured by the fluorescence intensity emitted by pyrene-actin co-polymerized into filaments for 1 h in a SpectraMax Gemini XS spectrofluorometer (Molecular Devices) at 355 nm excitation and 405 nm emission (44).

Adherens junction staining

Adherens junction staining was performed as described previously (45). Briefly, HRMVECs were grown to a confluent monolayer on cell culture-grade glass coverslips, quiesced, and treated with and without VEGFA (40 ng/ml) for 4 h. After treatments, cells were washed with cold PBS, fixed with 95% ethanol for 30 min at 4°C, permeabilized in TBS (10 mM Tris-HCl, pH 8.0, 150 mM NaCl) containing 0.1% Triton X100 for 10 min at room temperature and blocked with 2% BSA in TBS containing 10 mM $CaCl_2$, 5 mM $MgCl_2$, and 0.1% saponin overnight at 4°C. After incubation with the appropriate primary antibody (1:200 dilution) overnight, Alexa Flour-conjugated secondary antibody was added (1:500 dilution) and incubation continued for 1 h at room temperature, counterstained with Hoechst 33342 (1:1000 dilution in PBS) for 4 min and mounted onto glass slides with Prolong Gold antifade mounting medium. Wherever plasmids were used, cells were transfected with the indicated plasmid and 36 h later, these cells were seeded onto the coverslips. Fluorescence images of the cells were observed under a Zeiss inverted microscope (Axiovision Observer.z1; 40X/NA 0.6 or 10X/ NA 0.45), and the fluorescence images captured by a Zeiss AxioCam MRm camera using the microscope operating and image analysis software Zen 2.6 (blue edition).

Western blotting

After appropriate treatments, cell or retinal extracts were prepared and equal amounts of protein from control and each treatment were resolved by electrophoresis on SDS-polyacrylamide gels. The proteins were transferred electrophoretically onto a nitrocellulose membrane. After blocking in 5% (w/v) nonfat dry milk or BSA for 1 h, the membranes were incubated with indicated primary antibodies overnight at 4°C. Membranes were then washed with TBST 3X, 10 minutes each, followed by incubation with horseradish peroxidase-conjugated secondary antibody for 1 h. After washing again with TBST for 3X for 10 minutes each, membranes were incubated with enhanced chemiluminescence reagents (Amersham Biosciences), and the antigen-antibody complexes detected by exposure to X-ray film and developed in an X-ray film developer.

Transfections

HRMVECs were transfected with plasmid DNA (1 μg/ml) using Lipofectamine 3000 transfection reagent according to the manufacturer’s instructions. After 6 h of incubation, cells were recovered in EGM for 30 h, synchronized overnight in EBM, and used as needed.

Oxygen-induced retinopathy (OIR)

OIR was performed as per the method of Smith et al. (46) and quantified as per the protocol of Connor et al. (47) and as described by us previously (45). C57BL/6J and Cortactin$^{flox/flox}$:Cdh5-Cre^{ERT2} mice pups at post-natal day 7 (P7) along with their dams were exposed to 75% oxygen for 5 days (P7-P12) and then returned to room air at P12 to develop relative hypoxia (post-OIR). Mice pups of the same age kept at room air were used as controls. All the pups were euthanized at P17, and eyes enucleated and fixed in 4% (w/v) paraformaldehyde for 1 h at room temperature. Retinas were isolated, stained with isolectin B4, flat mounts were made, placed on a coverslip, and

examined under a Zeiss inverted fluorescence microscope (Axiovision Observer.z1). Retinal neovascularization was quantified by first setting a scale with a tolerance point of 50 based on the fluorescence intensity in the screenshot using Nikon NIS-Elements software version AR31. Neovascularity was highlighted in red (pseudo color) and then quantified by dividing the fluorescence intensity in the highlighted area by the total fluorescence intensity in the screenshot. When eyes were transfected with plasmid DNA, the pups' eyes were injected intravitreally with the indicated plasmid DNA at 1 μg/0.5 μl/eye using a 33G needle. Plasmid DNAs were prepared by mixing an equal volume of plasmid DNA (4 μg/μl) with an equal volume of complexation buffer, which was then mixed with an equal volume of Invivofectamine 3.0 transfection reagent (Thermo Fisher). The invivofectamine and plasmid mixtures were then incubated at 50°C for 30 minutes and diluted six times with PBS. The resulting mixture was then concentrated using Amicon Ultra-15 Ultracel-50K filters to achieve a final concentration of plasmid DNA to 2.0 μg/μl. Unless stated, mice pups with almost similar body weight (± 5%) were used in the study and both eyes of a pup received the same treatment.

Immunofluorescence staining

Normoxic and hypoxic (post-OIR) eyes were enucleated, fixed in 4% PFA, placed into OCT compound and cut 8-μm sections from the central part of the retina. After blocking in normal goat serum, the retinal sections were incubated with an indicated primary antibody raised in rabbit or mouse in combination with a rat anti-CD31 antibody at 1:100 dilution followed by incubation with Alexa Fluor 568-conjugated goat anti-rabbit/mouse and Alexa Fluor 488-conjugated goat anti-rat secondary antibodies. The sections were then observed under a Zeiss inverted microscope (Axiovision Observer.z1; 40X/NA 0.6 or 10X/NA 0.45) and the fluorescence images captured by a Zeiss AxioCam MRm camera using the microscope operating and image analysis software Zen 2.6 (blue edition).

Avascular area

The avascular area was calculated as per the method of Connor et al. (47). Briefly, images of post-OIR retinal flat mounts stained with isolectin B4 were obtained using Zeiss AxioObserver.Z1 microscope and AxioCam MRm camera were opened in Adobe Photoshop V. 23.4. Polygonal Lasso tool and the 'Add To Selection' function tool was used to obtain total retinal area. Using the same tools, the avascular area (i.e., vaso-obliterated area) was highlighted in white color. Once the total and avascular areas were outlined, then with the help of a 'Refresh' key, the number of pixels in those areas was recorded. The avascular area was calculated by dividing the pixels in the avascular area by pixels in the total area and multiplying by 100.

Retinal EC actin assembly

After blocking in 5% normal goat serum, the cryosections of P15 normoxic and 72 h of post-OIR eyes were incubated with rat anti-CD31 antibody (1:100) overnight at 4°C followed, washed 4X with PBS and incubated with Alexa Fluor 488-conjugated goat anti-rat secondary antibody in combination with Alexa Fluor 568 Phalloidin (1:500). The sections were then observed under a Zeiss inverted microscope (Axiovision Observer.z1; 40X/NA 0.6 or 10×/ NA 0.45) and the fluorescence images captured by a Zeiss AxioCam MRm

camera using the microscope operating and image analysis software Zen 2.6 (blue edition) (Carl Zeiss Imaging Solutions GmbH). The actin polymerization as observed by Phalloidin staining in EC was expressed as CD-31/Phalloidin-positive cells/section.

Retinal EC filopodia-like protrusions

P15 normoxic and 72 h of post-OIR retinal flat mounts stained with isolectin B4 were observed under a Zeiss inverted microscope (Axiovision Observer.z1; 40×/NA 0.6 or 10X/NA 0.45) and the fluorescence images captured using a Zeiss AxioCam MRm camera and the microscope operating and image analysis software Zen 2.6 (blue edition) (Carl Zeiss Imaging Solutions GmbH). The filopodia-like extensions from ECs at the leading edge of the growing superficial vascular network (vascular front) were counted using NIH ImageJ version 1.53 software and expressed as filopodia-like protrusions/100 μm vessel length.

Retinal vascular permeability assay

Retinal vascular permeability assay was performed as per the method of Vähätupa et al. (48). Briefly, C57BL/6J and Cortactin$^{flox/flox}$:Cdh5-Cre^{ERT2} mice pups were subjected to OIR, and at 96 h post-OIR (P16), pups were injected with 100 μl of 1% Evans Blue (EB) intraperitoneally or FITC-dextran (200 μg/ml) intravenously via tail vein. Twenty-four hours later (i.e., at P17), pups were euthanized, eyes enucleated, fixed and retinas isolated. Retinas from EB-injected pups were photographed and weighed. Then, EB was eluted from the retinas by incubation in 200 μl of N, N-dimethylformamide overnight at 78°C with gentle shaking. The supernatants were collected after centrifugation at 17000g for 45 minutes at 4°C, and the absorbance was measured in a spectrophotometer at 620 nm. Using a standard curve for EB, the EB concentration in the retina was calculated and normalized to the weight of the retina (49). The extravasation of the EB was presented in μg/retina. In the case of FITC-dextran extravasation assay, eyes were enucleated, fixed, retinas isolated, and stained with Hoechst 33342 (1:1000 dilution in PBS) for 30 min at room temperature. Subsequently, flat mounts were made, placed on a coverslip, examined under a Zeiss inverted fluorescence microscope (Axiovision Observer.z1), and the images were captured using a Zeiss AxioCam MRm camera. FITC-dextran extravasation was quantified by measuring the fluorescence intensity in the images by NIH ImageJ v1.53 software and presented as fold changes in the fluorescence intensity compared to normoxic retinas.

Miles' assay

Vascular permeability was performed as per the method of Brash et al. (50). Briefly, 8 wks of Cortactin$^{+/+}$ and Cortactin$^{i\Delta EC}$ mice were injected by ip with histamine inhibitor pyrilamine maleate (40 μg/gram body weight in saline) followed by i.v. injection of 100 μl of 1% (w/v in saline) EB via tail vein. The mice were placed on a 37°C heat plate for 30 min to circulate the dye. The mice were anesthetized, and 20 μl of VEGFA (2.5 μg/ml) was injected intradermally into the left flank at 3 sites, 1 cm apart from each other. PBS was injected into the right flanks of the same mice to serve as a vehicle control. After 20 minutes of intradermal injections of PBS or VEGFA, the mice were euthanized, pinned onto a board, subjected to a vertical incision of approximately 3 to 4 cm from the lower abdomen up to the chest, followed by teasing away the skin from both flanks with photos taken using a camera to visualize the EB leakage into the skin. Then, equally sized skin regions where PBS or

VEGFA were injected were cut and dried overnight at 55 °C. The EB was extracted from the skin samples with 250 μl of formamide and the absorbance measured as described above.

Statistics

Since mouse pups from P6 to P17 were used in the OIR experiments and the pups are sexually immature, sex differences were not expected to influence the observations. Therefore, OIR experiments were not performed in a gender-specific manner. Regarding Miles' assay, which was performed in adult mice, no gender differences were observed as analyzed by 2-tailed Student t test at $p<0.05$ and therefore the data were combined and presented. All the cell culture experiments were repeated three times, and the data presented as Mean ± SD. D'Agostino-Pearson and F-tests were used to determine the normality of the data and the equality of group variance, respectively, with GraphPad Prism v 8.00 software (https://www.graphpad.com/features) and the present data satisfied these two measures. Normally distributed data with similar variance were analyzed by 1-way ANOVA followed by Fisher's least significant difference post hoc test or 2-tailed Student t test with p values <0.05 considered as statistically significant. The group size for mice was determined by priori power analysis, where $\alpha = 0.05$, $\beta = 0.20$ and power = 0.80.

RESULTS

Cortactin phosphorylation at Y470 is required for VEGFA-induced HRMVEC angiogenic events in vitro and OIR-induced retinal neovascularization in vivo.

Cortactin plays an important role in F-actin formation and its stabilization, which is a critical factor in actin cytoskeletal remodeling (26, 51). Many studies have reported that cytoskeletal remodeling is required for cell migration, proliferation, and differentiation (52–54). Since VEGFA plays a pivotal role in physiological and pathological angiogenesis by stimulating EC migration, proliferation, and differentiation (55, 56), we asked whether cortactin has any role in VEGFA-induced EC angiogenic responses. To this end, first, we studied the time-course effect of VEGFA on cortactin tyrosine phosphorylation. We found that VEGFA induces tyrosine phosphorylation of cortactin in a time-dependent manner with maximum effect at 30 min and declining thereafter in HRMVECs (Figure 1A). Previously, we and others have reported the presence of several tyrosine phosphorylation sites in human cortactin (37, 51, 57, 58). In consideration of these observations, we next wanted to identify the tyrosine residue(s) that was phosphorylated in HRMVECs by VEGFA. Using mutants for the potential phosphorylation sites (37), we found that VEGFA induces cortactin phosphorylation at Y421, Y453, and Y470 residues (Figure 1B). Since cortactin is an actin-binding protein and involved in F-actin formation (26), we tested whether phosphorylation of cortactin at these sites has any link to actin assembly. We found that VEGFA induces actin polymerization and that cortactin Y470F but not Y421F or Y453F mutant attenuates this effect (Figure 1C). Thus, cortactin appeared to promote the formation of stress fibers in HRMVECs upon treatment with VEGFA. Interestingly, expression of cortactin Y470F mutant suppressed VEGFA-induced F-actin stress fiber formation by ~65% (Figure 1D). Previous studies have reported that cortactin interacts with Arp2/3 complex in the regulation of actin polymerization (59). Based on these observations, we tested whether phosphorylation of cortactin at Y470 was required for its interaction with Arp2/3 complex.

We found that in response to VEGFA, cortactin interacts with Arp2/3 and that expression of cortactin Y470F mutant blocks this interaction by >70% (Figure 1E). In addition, inhibition of Arp2/3 complex by CK666 (60) blocked VEGFA-induced actin polymerization completely (Figure 1F). These observations indicated that cortactin phosphorylation at Y470 residue is required for VEGFA-induced actin polymerization and stress fiber formation. Cortactin has been reported to play a role in cell migration and proliferation (23, 24, 37). In lieu of these observations, we next studied the role of cortactin tyrosine phosphorylation in VEGFA-induced HRMVEC migration and proliferation. While expression of cortactin variants deficient for phosphorylation at Y421 or Y453 had little effect, the mutant that prevents phosphorylation at Y470 residue suppressed VEGFA-induced HRMVEC migration by ~75% and proliferation by ~55% (Figure 2A & B). Because lamellipodia formation is required for cell migration (41), we next tested the effect of cortactin Y470F mutant on VEGFA-induced HRMVEC lamellipodia formation. As expected, overexpression of cortactin Y470F mutant attenuated VEGFA-induced HRMVEC lamellipodia formation substantially, a finding that confirms the role of cortactin Y470 phosphorylation in VEGFA-induced HRMVEC migration (Figure S2). Regarding the mechanism by which cortactin modulates VEGFA-induced EC proliferation, previously we reported that CDC6 interacts with cortactin (61). CDC6 is an essential component of pre-replication complex that plays an indispensable role in DNA replication (62). Therefore, we first studied a time course effect of VEGFA on cortactin interaction with CDC6. VEGFA induced cortactin interaction with CDC6 in a manner that correlates with its tyrosine phosphorylation (Figure S3A & Figure 1A). Furthermore, coimmunofluorescence staining revealed that cortactin interaction with CDC6 occurs in the cytoplasm from 30 min to 60 min, and later the CDC6 appears only in the nucleus leaving cortactin in the cytoplasm, mostly perinuclear (Figure S3B). Next, we found that cortactin Y470F mutant blocks VEGFA-induced cortactin interaction with CDC6 (Figure S3C). Not only overexpression of cortactin Y470F mutant blocked cortactin interaction with CDC6, but also prevented VEGFA-induced CDC6 translocation from the cytoplasm to the nucleus (Figure S3D). Corroborating the role of cortactin phosphorylation at Y470 in VEGFA-induced EC migration and proliferation, blockade of cortactin phosphorylation at Y470 also inhibited VEGFA-induced HRMVEC sprouting and tube formation (Figure 2C & D). To extrapolate these observations to an *in vivo* setting, we used an OIR model (46, 47). Mouse pups with dams (mothers) were either left at room air (normoxia) or in a hyperoxic chamber from postnatal day 7 (P7) to P12 and returned to room air at P12 to develop relative hypoxia (hereon referred to as post-OIR). To study the role of cortactin tyrosine phosphorylation in OIR-induced retinal neovascularization, normoxic and hyperoxic mouse pups were injected intravitreally with pCMV, pCMV-Cttn (WT) or pCMV-Cttn (Y470F) expression plasmids at P10 and P11 for determination of cortactin phosphorylation, and at P10, P11, and P13 to examine retinal neovascularization. As shown in Figure 3A (bottom panel), phosphorylation of cortactin at Y466, a murine equivalent to human cortactin Y470 residue (63), was found to be induced very robustly in mouse retinas at 24-h post-OIR as compared to normoxic retinas. In line with the *in vitro* observations in HRMVECs, overexpression of cortactin Y470F mutant also attenuated OIR-induced cortactin tyrosine phosphorylation in mouse retinas (Figure 3A, bottom panel). Furthermore, overexpression of Y470F mutant suppressed OIR-induced actin assembly by ~60% in retinal ECs as measured by fluorescence microscopy of retinal cross sections

stained with phalloidin and CD31 (Figure 3B). In addition, overexpression of cortactin Y470F mutant inhibited OIR-induced EC filopodia-like protrusions and proliferation (Figure 3C & D). Similarly, overexpression of cortactin Y470F mutant decreased vascular density and retinal neovascularization with an increase in avascular area (Figure 3E–G). It was interesting to note that overexpression of WT cortactin enhanced the effect of OIR on retinal neovascularization with an additive decrease in the avascular area (Figure 3B–G). In addition, expression of Cttn Y470F mutant delayed revascularization of OIR retinas at least until P23 (11 days post-OIR) as compared to pCMV control (Figure S4). In other words, at P23 (i.e., 11 days post-OIR), there was almost ~80% retinal revascularization in pCMV control, whereas in pCMV-Cttn (Y470F) transfected retinas, the revascularization reached only to 30%. Together, these results indicated that cortactin phosphorylation at Y470 is required for OIR-induced formation of EC filopodia-like protrusions, proliferation, and retinal neovascularization.

Cortactin phosphorylation at Y421 residue is required for disruption of adherens junctions leading to vascular leakage.

Endothelial cells by virtue of developing intercellular junctions such as adherens junctions (AJs) play an important role in the maintenance of vascular permeability (64–67). AJs are composed of protein complexes between VE-cadherin, a transmembrane protein, and its intracellular binding partners, namely α-, β-, γ-, and p120-catenins (64, 67). Besides its association with catenins, VE-cadherin also interacts with actin-binding proteins directly or via α-catenin in the maintenance of cytoskeletal stability (67, 68). Based on these clues and the fact that cortactin is an actin-binding protein, we wanted to find whether cortactin interacts with VE-cadherin. Interestingly, under resting conditions, cortactin was found to be in a complex with VE-cadherin in HRMVECs, and in response to VEGFA, it dissociated from VE-cadherin in a time-dependent manner (Figure 4A). Many studies have reported a role for post-translational modifications such as phosphorylation of VE-cadherin and catenins in the regulation of AJ stability (69–71). As VEGFA disrupts AJs (72) and phosphorylates cortactin at Y421, Y453, and Y470 residues (present study), we next studied the role of cortactin tyrosine phosphorylation in EC barrier function. As expected, VEGFA decreased trans-endothelial resistance (TER) of the HRMVEC monolayer in a time-dependent manner (Figure 4B). In addition, overexpression of cortactin Y421F but not Y453F or Y470F mutant prevented the decrease in TER in response to VEGFA (Figure 4B). In line with these observations, VEGFA increased dextran flux through the HRMVEC monolayer in a time-dependent manner as compared to vehicle control, and overexpression of cortactin Y421F mutant prevented this effect (Figure 4C). To find whether cortactin phosphorylation at Y421 residue was involved in the disruption of its association with VE-cadherin, next, we tested the effect of cortactin Y421F mutant on cortactin-VE-cadherin interactions. Overexpression of cortactin Y421F mutant protected cortactin and VE-cadherin complex from their disruption by VEGFA in HRMVECs (Figure 4D). In line with these observations, overexpression of cortactin Y421F mutant also protected AJs from VEGFA-induced disruption by >70% (Figure 4E). Together, these results indicated that cortactin phosphorylation at Y421 is involved in VEGFA-induced disruption of HRMVEC AJs and its barrier function. To extrapolate the involvement of cortactin Y421 phosphorylation in EC barrier function *in vivo*, we examined its role in vascular leakage. WT mouse pups

with dams were housed in normoxia or in a hyperoxia chamber from P7 to P12 and at P10, P11 and P13, the pups were given intravitreal injections of pCMV, pCMV-Cttn (WT) or pCMV-Cttn (Y421F) expression plasmids. The pups that were exposed to hyperoxia were then returned to room air at P12 to develop relative hypoxia. At P13, retinas were isolated and examined for cortactin phosphorylation at Y421. We found that in pups that received pCMV alone and subjected to OIR, the retinas showed increased phosphorylation of cortactin at Y421 and this response was completely negated in the retinas of pups that received pCMV-Cttn (Y421F) mutant (Figure 5A & B). To test the role of cortactin Y421 phosphorylation in vascular leakage, at P16, the pups were injected by i.p. with Evans blue, and 24-h later, the eyes from the pups were enucleated, fixed, retinas isolated, and Evans blue extravasation measured. OIR induced retinal vascular leakage as observed by Evans blue extravasation (Figure 5A & C). While overexpression of cortactin Y421F mutant suppressed retinal vascular leakage by >55%, overexpression of WT cortactin showed a 50% additive effect on vascular leakage (Figure 5C). It is noteworthy that overexpression of Cttn-(WT) also caused a small increase in vascular leakage in normoxic retinas as compared to vector control (Figure 5D). To further confirm the role of cortactin Y421 phosphorylation in retinal vascular leakage, we also used a FITC-dextran (70 kDa) extravasation approach. In line with the observations obtained using Evans blue, the FITC-dextran approach also yielded similar results in normoxic and OIR-induced retinal vascular leakage (Figure 5E). Consistent with its lack of a role in VEGFA-induced HRMVEC migration, proliferation, sprouting and tube formation, forced expression of Cttn (Y421F) mutant had no effect on OIR-induced retinal neovascularization (Figure S5). Together, these observations indicated a role for cortactin Y421 phosphorylation in retinal vascular leakage.

Lyn and Syk via mediating cortactin Y470 and Y421 phosphorylation modulate retinal neovascularization and vascular leakage, respectively.

Previous studies have shown that small G proteins such as Rac1 and RhoA play a crucial role in cytoskeletal remodeling (73, 74). Since cortactin is an actin-binding cytoskeletal protein, we first studied the role of Rac1 and RhoA in VEGFA-induced cortactin tyrosine phosphorylation. Depletion of either Rac1 or RhoA levels by their target siRNAs had no effect on VEGFA-induced cortactin tyrosine phosphorylation in HRMVECs (Figure S6). Due to the lack of a role for Rac1 and RhoA in VEGFA-induced cortactin tyrosine phosphorylation, we next examined the role of tyrosine kinases. We found that VEGFA stimulates tyrosine phosphorylation of Src, Lyn, Syk, and Pyk2 more robustly and Yes and Fak moderately in a time-dependent manner with maximum effects at 30 min and declining thereafter in HRMVECs (Figure 6A). No apparent changes were observed in the phosphorylation of Btk, Fyn and Frk between control and VEGFA-treated cells (Figure 6A). As VEGFA activated Src, Lyn, Syk and Pyk2 more robustly than Yes and Fak, we next studied their role in VEGFA-induced cortactin Y421 and Y470 phosphorylation. We found that siRNA-mediated depletion of Lyn but not Src completely blocked VEGFA-induced cortactin Y470 phosphorylation (Figure 6B). Inhibition of either Syk or Pyk2 had no effect on VEGFA-induced cortactin Y470 phosphorylation (Figure 6C). On the other hand, inhibition of Syk but not Pyk2 attenuated cortactin Y421 phosphorylation by VEGFA (Figure 6B & C). Downregulation of either Lyn or Src had no effect (Figure 6B & C). These findings revealed that different tyrosine kinases are involved in the phosphorylation

of cortactin at different tyrosine residues in response to VEGFA. Consistent with these observations, OIR also induced tyrosine phosphorylation of Lyn and Syk in the mouse pup retinas in a time-dependent manner with maximum effects at 12 h post-OIR and decreasing thereafter (Figure 6D). In addition, while lentivirus-mediated expression of shRNA targeting Lyn depletion blocked cortactin phosphorylation at Y466, an equivalent of Y470 residue in humans (63), shRNA targeting Syk downregulation suppressed OIR-induced cortactin phosphorylation at Y421 residue (Figure 6E). Based on the role of Lyn and Syk in cortactin Y470 and Y421 phosphorylation, respectively, we next studied their roles in retinal neovascularization and vascular leakage. OIR-induced EC filopodia-like protrusions and retinal neovascularization in mouse pup retinas were reduced substantially (>60%) upon shRNA-mediated depletion of Lyn levels, coinciding with increased avascular areas as compared to control pup retinas (Figure 7A–C). On the other hand, OIR-induced retinal vascular leakage was attenuated by shRNA-mediated depletion of Syk levels as compared to their respective controls (Figure 7D & E). These observations thus supported a role for Lyn and Syk in the phosphorylation of cortactin at residues Y470 and Y421 in mediating retinal neovascularization and vascular leakage, respectively.

EC-specific deletion of cortactin suppresses OIR-induced retinal neovascularization and vascular leakage.

To relate that cortactin tyrosine phosphorylation at different sites in ECs was involved in retinal neovascularization and vascular leakage, we used EC-specific cortactin knockout mice. Cortactin$^{flox/flox}$:Cdh5-Cre^{ERT2} mouse pups with dams were housed in normoxia or in a hyperoxia chamber from P7 to P12 and returned to room air at P12 to develop relative hypoxia. Nuclear Cre was induced by tamoxifen injection at P9 and P11 to generate EC-specific cortactin knockout pups (now onwards referred to as Cortactin$^{i\Delta EC}$ pups). The eyes from normoxic and 72-h and 120-h post-OIR pups were enucleated, fixed, retinas isolated, and analyzed for neovascularization. At the same time, tail clips (2 mm) were collected from these pups and genotyped for Cortactin$^{flox/flox}$ and Cdh5-Cre^{ERT2} allele. Mouse pups that were positive for both Cortactin$^{flox/flox}$ and Cdh5-Cre^{ERT2} allele were considered as Cortactin$^{i\Delta EC}$ and those which were positive for Cortactin$^{flox/flox}$ and negative for Cdh5-Cre^{ERT2} allele were considered as Cortactin$^{flox/flox}$ pups. Coimmunostaining for cortactin along with CD31 showed that cortactin levels were completely depleted only in the ECs of both normoxic and post-OIR retinas of Cortactin$^{i\Delta EC}$ mouse pups as compared to retinas of Cortactin$^{flox/flox}$ mouse pups (Figure 8A, bottom panel). We next examined the role of EC-specific cortactin deletion in OIR-induced actin assembly in the retinal ECs of these mouse pups. As expected, coimmunostaining of retinal cross sections for phalloidin and CD31 showed that actin assembly was induced prominently in ECs of 72-h post-OIR Cortactin$^{flox/flox}$ mouse pup retinas, and this effect was blunted in Cortactin$^{i\Delta EC}$ mouse pup retinas (Figure 8B). Consistent with these observations, EC-specific deletion of cortactin also reduced EC filopodia-like protrusions, EC proliferation, and retinal neovascularization resulting in increased avascular area as compared to Cortactin$^{flox/flox}$ mouse pup retinas (Figure 8C–G). Regarding vascular leakage, we used two approaches. In the first approach, Cortactin$^{flox/flox}$:Cdh5-Cre^{ERT2} mouse pups with dams were housed in normoxia or in a hyperoxia chamber from P7 to P12 and returned to room air at P12. Cre was induced in pups by tamoxifen injections at P9 and P11. Normoxic (P16) and 96-h post-OIR mouse

pups (P16) were injected with Evans blue by i.p. or FITC-dextran by i.v. and 24-h later the eyes from these pups were enucleated, fixed, retinas isolated, and examined for retinal vascular leakage. EC-specific deletion of cortactin blunted OIR-induced vascular leakage by >60% as observed by reduced Evans blue/FITC-dextran extravasation (Figure 8H & I). In the second approach, we used adult mice to evaluate cortactin's role in VEGFA-induced vascular hyperpermeability in the skin by Mile's assay. VEGFA-induced Evans blue hyperpermeability in the skin of cortactin$^{flox/flox}$ mice and EC-specific deletion of cortactin blunted this effect by >75% (Figure 8J). Thus, these results demonstrate the involvement of EC-specific cortactin in mediating OIR-induced retinal neovascularization and vascular leakage.

DISCUSSION

DR negatively impacts the quality of life, mental health and accelerates the fear of vulnerability with loss of independence, self-care, and mobility (75, 76). Vision loss in DR is primarily due to hypoxia, retinal hyperpermeability, and neovascularization which eventually leads to anatomical and functional alterations in retinal cells (9, 11, 13, 48, 77). In treating DR, medical interventions such as pan-retinal photocoagulation (PRP) surgeries and anti-VEGF therapies have emerged as effective approaches (78). In contrast to PRP, which seems to be a one-time procedure in patients with DR (79), the anti-VEGF therapy requires near-monthly follow-up and injection regimen for adequate treatment for prevention of PDR recurrency (13). Therefore, new therapies that are more targeted, potent, and/or long-lasting are required for treating PDR.

To this end, our results demonstrate for the first time that cortactin, a key scaffold actin-binding protein, plays a crucial role in OIR-induced retinal neovascularization. In validating a full-blown role of cortactin in retinal angiogenesis, we found that cortactin was phosphorylated on tyrosine residues both in VEGFA-treated HRMVECs and in post-OIR retinas. These findings may infer that cortactin tyrosine phosphorylation was involved in VEGFA and OIR-induced angiogenesis. It is also noteworthy that VEGFA induces tyrosine phosphorylation of cortactin at Y421, Y453, and Y470 residues, perhaps in mediating different aspects of angiogenic events. Previous studies have reported that tyrosine phosphorylation of cortactin was required for promoting actin polymerization (80). In this context, our findings reveal that among the three tyrosine residues phosphorylated by VEGFA, phosphorylation of cortactin at Y470 residue was required for its interaction with Arp2/3 complex in the modulation of VEGFA-induced actin polymerization and stress fiber formation. Increased actin assembly and stress fiber formation have been associated with cell stiffness, an important factor in the modulation of cell migration, whereas a reduction in its polymerization correlates with reduced cell stiffness (81). The canonical, so-called ventral stress fibers are not only directly connected to and thus anchored in cell-matrix adhesions, allowing cells to stabilize their protrusions, but also able to drag themselves forward during directional migration (82). However, excess stress fiber formation can also counteract efficient migration due to unproductive, over-emphasized spatial immobilization of migrating cells, so these processes must be well balanced. In any case, our observations reveal that among the three sites of cortactin phosphorylated by VEGFA, blockade of phosphorylation at Y470 residue by cortactin Y470F mutant blocked VEGFA-induced

HRMVEC migration. In fact, expression of cortactin Y470F mutant also blocked VEGFA-induced lamellipodia formation in HRMVECs, a finding that confirms the involvement of cortactin phosphorylation at Y470 in EC migration. Stress fiber formation has also been shown to be involved in cell proliferation and differentiation (82–84). Indeed, our findings show that phosphorylation of cortactin at Y470 residue that promoted actin assembly and stress fiber formation was also involved in VEGFA-induced HRMVEC proliferation, sprouting, and tube formation. Regarding the possible mechanism by which cortactin modulates VEGFA-induced EC proliferation, our results revealed that cortactin interacts with CDC6 and promotes its nuclear import and that these effects were dependent on phosphorylation of cortactin at Y470 residue. Cortactin phosphorylation at Y470 residue was not only required for VEGFA-induced HRMVEC stress fiber formation, but also involved in OIR-induced F-actin formation in retinal ECs, suggesting the role of cortactin Y470 phosphorylation in angiogenic responses during OIR. Notably, since the formation of filopodia-like protrusions is one of the characteristic features of tip cells (85), we also studied the effect of cortactin Y470F mutant on these processes in OIR-induced retinal ECs. Our results suggest that OIR-induced formation of filopodia-like protrusions in ECs of pup's retinas also requires cortactin phosphorylation at Y470. EC migration and proliferation are essential for tip cell formation in the development of new blood vessels (56). In this regard, our observations show that forced expression of cortactin Y470F mutant blunts OIR-induced EC proliferation and neovascularization with increased avascular area in the retinas of these pups. On the other hand, forced expression of WT cortactin had additive effects on EC proliferation and retinal neovascularization with decreased avascular area. This additive effect could be due to heightened cortactin phosphorylation at Y466 (Y470 in humans), which in turn, increases stress fiber formation and neovascularization. Aside from this, the involvement of cortactin in OIR-induced retinal neovascularization was further supported by the findings that EC-specific knockout of cortactin substantially reduced F-actin and formation of filopodia-like protrusions in OIR-induced retinal ECs, EC proliferation, as well as neovascularization. Thus, the avascular area was also increased in the retinas of these mouse pups. Since blockade of cortactin Y466/Y470 phosphorylation in OIR retinas delayed retinal revascularization at least by 120 h as compared to vector control, it appears that cortactin phosphorylation at this site is crucial for retinal neovascularization. Together, these observations clearly suggest that cortactin phosphorylation at Y470 residue is required for both VEGFA and OIR-induced EC angiogenic responses.

EC can form lamellipodia as initial contacts with the extracellular matrix and, frequently combined with filopodia-like bridges, develop nascent, VE-cadherin-based junctions (86). Previous studies reported that cortactin is involved in E-cadherin-mediated cell-cell contact formation via its recruitment into cell adhesion sites and involvement in actin reorganization (87). Moreover, cortactin accumulates preferentially at the extending regions of cadherin-adhesive contact zones, and by interaction with Arp2/3 was proposed to participate in actin remodeling at these contacts (87). Thus, cortactin can play important roles in the biogenesis of adherens junctions (87) and thus in barrier function (38). To this end, our findings reveal that cortactin interacts with VE-cadherin in the resting state and operates in the maintenance of AJ integrity and EC barrier function, but in response to VEGFA, it dissociates from VE-Cadherin coinciding with disruption of AJs and barrier integrity. Since the Y421F mutant

of cortactin prevented these effects, it appears that the phosphorylation of cortactin at this residue is required for VEGFA-induced disruption of VE-cadherin-cortactin interactions, affecting AJ integrity and EC barrier function. The observation that phosphorylation at Y453 or Y470 residues had no effect on VEGFA-induced VE-cadherin interactions, AJ integrity and EC barrier function confirmed the site-specificity of cortactin phosphorylation in these events. These conclusions were further supported by our findings that cortactin Y421F mutant also restored OIR-induced retinal vascular leakage in murine WT pups. Similarly, EC-specific deletion of cortactin in mice attenuated OIR-induced retinal vascular leakage as well as VEGFA-induced vascular hyperpermeability. In addition, the role of cortactin in vascular leakage appears to be mediated by its site-specific phosphorylation, as blockade of its phosphorylation at Y421 residue had no effect on OIR-induced neovascularization. Thus, the present observations suggested that cortactin phosphorylation at Y421 leads to its dissociation from VE-cadherin, affecting AJ integrity and thereby increasing vascular permeability in response to VEGFA/OIR. Regarding the role of cortactin Y453 phosphorylation, it had no effect on VEGFA-induced EC angiogenic responses such as migration, proliferation, sprouting, tube formation or EC monolayer barrier function. It might be possible that cortactin phosphorylation at Y453 is involved in other EC responses such as cell to cell interactions that needs to be investigated.

In elucidating the upstream mechanisms by which VEGFA triggers cortactin phosphorylation at different sites, we found that without a role for small G proteins such as Rac1 and RhoA, Lyn mediates cortactin phosphorylation at Y470 residue and Syk mediates cortactin phosphorylation at Y421 residue. A large body of literature suggests that cortactin is a substrate for Src (88, 89). Besides this, a few studies also showed that cortactin can be a substrate for Lyn and Syk (90–92). However, these studies did not identify the specific phosphorylation sites of cortactin by Lyn or Syk. To this end, our observations show that Lyn and Syk not only phosphorylate cortactin at different sites, but also reveal that these phosphorylation sites have differential roles in mediating retinal neovascularization and vascular leakage. In line with their role in the phosphorylation of cortactin at Y470 and Y421, depletion of Lyn levels attenuated OIR-induced retinal neovascularization, and depletion of Syk blunted OIR-induced vascular leakage, respectively. As cortactin phosphorylation at Y421 is required for disruption of cortactin-VE-cadherin interactions and AJs, and Syk mediates cortactin phosphorylation at Y421, we conclude that Syk activation will mediate the disruption of AJ integrity leading to barrier dysfunction and vascular leakage. Together with the involvement of site-specific phosphorylation of cortactin in retinal neovascularization and vascular leakage, EC-specific cortactin deletion also suppressed OIR-induced retinal neovascularization and vascular leakage. Thus, all these observations support a role for EC-specific cortactin on VEGFA/OIR-induced retinal angiogenesis and vascular leakage.

CONCLUSIONS

As depicted in Figure 8K, the above observations suggest that while phosphorylation of cortactin at Y470 by Lyn is required for VEGFA/OIR-induced retinal neovascularization, its phosphorylation at Y421 residue by Syk is involved in contributing to vascular leakage. Therefore, cortactin could be a novel target for the development of therapeutics targeting

pathological retinal angiogenesis. Since two different phosphorylation sites were involved in retinal neovascularization and vascular leakage and both the events are characteristic features of PDR, use of decoy peptides targeting blockade of phosphorylation at both sites could be considered in the development of effective therapeutic agents against PDR.

Supplementary Material

Refer to Web version on PubMed Central for supplementary material.

Sources of funding:

This work was supported by the National Eye Institute grants EY014856 and EY034425 from the National Institutes of Health to GN Rao, and by intramural funding from the Helmholtz Society to K Rottner.

NONSTANDARD ABBREVIATIONS AND ACRONYMS

Cttn	Cortactin
DR	Diabetic retinopathy
EB	Evans blue
EBM	Endothelial basal medium
EC	Endothelial cell
EBM	Endothelial basal medium
EGM	Endothelial growth medium
HRMVEC	Human retinal microvascular endothelial cell
NPDR	Non-proliferative diabetic retinopathy
OIR	Oxygen-induced retinopathy
PDR	Proliferative diabetic retinopathy
VEGF	Vascular endothelial growth factor
VEGFA	Vascular endothelial growth factor A
VEGFR	Vascular endothelial growth factor receptor
WT	Wild type

REFERENCES

1. Peto T, Resnikoff S, Kempen JH, Steinmetz JD, Briant PS, Wong TY, Friedman DS, Bron AM, Jonas J, Fernandes A, et al. Diabetic retinopathy contributes to global vision loss. Invest. Ophthalmol. Vis. Sci 2021;62:1139.
2. World Health Organization. Regional Office for South-East Asia. Strengthening diagnosis and treatment of Diabetic Retinopathy in SEA Region. 2020; Available at: https://apps.who.int/iris/handle/10665/334224 (accessed Apr 17, 2023).

3. Centers for Disease Control and Prevention. National Diabetes Statistics Report. Atlanta, GA: Centers for Disease Control and Prevention, U.S. Dept of Health and Human Services; 2020; Available at: https://www.cdc.gov/diabetes/pdfs/data/statistics/national-diabetes-statistics-report.pdf (accessed Apr 17, 2023).
4. International Diabetes Federation. IDF Diabetes Atlas, 10th edn. Brussels, Belgium: 2021; Available at: https://www.diabetesatlas.org (accessed Apr 17, 2023).
5. Harris NK, Talwar N, Gardner TW, Wrobel JS, Herman WH, Stein JD. Predicting development of proliferative diabetic retinopathy. Diabetes Care. 2013;36:1562–1568. [PubMed: 23275374]
6. Solomon SD, Chew E, Duh EJ, Sobrin L, Sun JK, VanderBeek BL, Wykoff CC, Gardner TW. Diabetic Retinopathy: A Position Statement by the American Diabetes Association. Diabetes Care. 2017;40:412–418. [PubMed: 28223445]
7. Liu Y, Cox SR, Morita T, Kourembanas S. Hypoxia regulates vascular endothelial growth factor gene expression in endothelial cells. Identification of a 5' enhancer. Circ Res. 1995;77:638–643. [PubMed: 7641334]
8. Xu Q, Wang Y, Dabdoub A, Smallwood PM, Williams J, Woods C, Kelley MW, Jiang L, Tasman W, Zhang K, et al. Vascular development in the retina and inner ear: control by Norrin and Frizzled-4, a high-affinity ligand-receptor pair. Cell. 2004;116:883–895. [PubMed: 15035989]
9. Miloudi K, Oubaha M, Ménard C, Dejda A, Guber V, Cagnone G, Wilson AM, Tétreault N, Mawambo G, Binet F, et al. NOTCH1 signaling induces pathological vascular permeability in diabetic retinopathy. Proc Natl Acad Sci U S A. 2019;116:4538–4547. [PubMed: 30787185]
10. Sun JK, Radwan SH, Soliman AZ, Lammer J, Lin MM, Prager SG, Silva PS, Aiello LB, Aiello LP. Neural Retinal Disorganization as a Robust Marker of Visual Acuity in Current and Resolved Diabetic Macular Edema. Diabetes. 2015;64:2560–2570. [PubMed: 25633419]
11. Ferrara N VEGF and Intraocular Neovascularization: From Discovery to Therapy. Transl Vis Sci Technol. 2016;5:10.
12. Stitt AW, Curtis TM, Chen M, Medina RJ, McKay GJ, Jenkins A, Gardiner TA, Lyons TJ, Hammes HP, Simó R, et al. The progress in understanding and treatment of diabetic retinopathy. Prog Retin Eye Res. 2016;51:156–186. [PubMed: 26297071]
13. Maturi RK, Glassman AR, Josic K, Antoszyk AN, Blodi BA, Jampol LM, Marcus DM, Martin DF, Melia M, Salehi-Had H, et al. DRCR Retina Network. Effect of Intravitreous Anti-Vascular Endothelial Growth Factor vs Sham Treatment for Prevention of Vision-Threatening Complications of Diabetic Retinopathy: The Protocol W Randomized Clinical Trial. JAMA Ophthalmol. 2021;139:701–712. [PubMed: 33784735]
14. Gross JG, Glassman AR, Jampol LM, Inusah S, Aiello LP, Antoszyk AN, Baker CW, Berger BB, Bressler NM, Browning D, et al. Panretinal Photocoagulation vs Intravitreous Ranibizumab for Proliferative Diabetic Retinopathy: A Randomized Clinical Trial. JAMA. 2015;314:2137–2146. [PubMed: 26565927]
15. Bressler SB, Qin H, Melia M, Bressler NM, Beck RW, Chan CK, Grover S, Miller DG. Diabetic Retinopathy Clinical Research Network. Exploratory analysis of the effect of intravitreal ranibizumab or triamcinolone on worsening of diabetic retinopathy in a randomized clinical trial. JAMA Ophthalmol. 2013;131:1033–1040. [PubMed: 23807371]
16. Smith Q, Rochman N, Carmo AM, Vig D, Chan XY, Sun S, Gerecht S. Cytoskeletal tension regulates mesodermal spatial organization and subsequent vascular fate. Proc Natl Acad Sci U S A. 2018;115:8167–8172. [PubMed: 30038020]
17. Janmey PA. Creating a niche in the cytoskeleton: Actin reorganization by a protein kinase. Proc Natl Acad Sci U S A. 2001;98:14745–14747. [PubMed: 11752415]
18. Osborn EA, Rabodzey A, Dewey CF Jr, Hartwig JH. Endothelial actin cytoskeleton remodeling during mechanostimulation with fluid shear stress. Am. J. Physiol. Cell Physiol 2006;290:C444–C452. [PubMed: 16176968]
19. Mcgrath JL, Osborn EA, Tardy YS, Dewey CF Jr, Hartwig JH. Regulation of the actin cycle in vivo by actin filament severing. Proc. Natl. Acad. Sci. USA. 2000;97:6532–6537. [PubMed: 10823888]
20. Disanza A, Steffen A, Hertzog M, Frittoli E, Rottner K, Scita G. Actin polymerization machinery: the finish line of signaling networks, the starting point of cellular movement. Cell Mol Life Sci. 2005;62:955–970. [PubMed: 15868099]

21. Mitchison TJ, Cramer LP. Actin-based cell motility and cell locomotion. Cell. 1996;84:371–379. [PubMed: 8608590]
22. Zigmond SH. How WASP regulates actin polymerization. J Cell Biol. 2000;150:F117–120. [PubMed: 10995455]
23. Clark ES, Whigham AS, Yarbrough WG, Weaver AM. Cortactin is an essential regulator of matrix metalloproteinase secretion and extracellular matrix degradation in invadopodia. Cancer Res. 2007;67:4227–4235. [PubMed: 17483334]
24. Nürnberg A, Kitzing T, Grosse R. Nucleating actin for invasion. Nat Rev Cancer. 2011;11:177–187. [PubMed: 21326322]
25. Goley ED, Welch MD. The ARP2/3 complex: an actin nucleator comes of age. Nat Rev Mol Cell Biol. 2006;7:713–726. [PubMed: 16990851]
26. Weaver AM, Karginov AV, Kinley AW, Weed SA, Li Y, Parsons JT, Cooper JA. Cortactin promotes and stabilizes Arp2/3-induced actin filament network formation. Curr Biol. 2001;11:370–374. [PubMed: 11267876]
27. Weaver AM. Cortactin in tumor invasiveness. Cancer Lett. 2008;265:157–166. [PubMed: 18406052]
28. Campbell DH, deFazio A, Sutherland RL, Daly RJ. Expression and tyrosine phosphorylation of EMS1 in human breast cancer cell lines. Int J Cancer. 1996;68:485–492. [PubMed: 8945620]
29. Cai JH, Zhao R, Zhu JW, Jin XL, Wan FJ, Liu K, Ji XP, Zhu YB, Zhu ZG. Expression of cortactin correlates with a poor prognosis in patients with stages II-III colorectal adenocarcinoma. J Gastrointest Surg. 2010;14:1248–1257. [PubMed: 20532661]
30. Chen JH, Chen KY, Ma HI, Yu CP, Nieh S, Lee HS, Jin JS. Cortactin, fascin and survivin expression associated with clinicopathological parameters in brain gliosarcoma. Chin J Physiol. 2010;53:234–244. [PubMed: 21793333]
31. Faoro L, Singleton PA, Cervantes GM, Lennon FE, Choong NW, Kanteti R, Ferguson BD, Husain AN, Tretiakova MS, Ramnath N, et al. EphA2 mutation in lung squamous cell carcinoma promotes increased cell survival, cell invasion, focal adhesions, and mammalian target of rapamycin activation. J Biol Chem. 2010;285:18575–18585. [PubMed: 20360610]
32. Xu XZ, Garcia MV, Li TY, Khor LY, Gajapathy RS, Spittle C, Weed S, Lessin SR, Wu H. Cytoskeleton alterations in melanoma: aberrant expression of cortactin, an actin-binding adapter protein, correlates with melanocytic tumor progression. Mod Pathol. 2010;23:187–196. [PubMed: 19898426]
33. Akervall JA, Jin Y, Wennerberg JP, Zätterström UK, Kjellén E, Mertens F, Willén R, Mandahl N, Heim S, Mitelman F. Chromosomal abnormalities involving 11q13 are associated with poor prognosis in patients with squamous cell carcinoma of the head and neck. Cancer. 1995;76:853–859. [PubMed: 8625189]
34. García-Castillo J, Pedersen K, Angelini PD, Bech-Serra JJ, Colomé N, Cunningham MP, Parra-Palau JL, Canals F, Baselga J, Arribas J. HER2 carboxyl-terminal fragments regulate cell migration and cortactin phosphorylation. J Biol Chem. 2009;284:25302–25313. [PubMed: 19589785]
35. Wu H, Reynolds AB, Kanner SB, Vines RR, Parsons JT. Identification and characterization of a novel cytoskeleton-associated pp60src substrate. Mol Cell Biol. 1991;11:5113–5124. [PubMed: 1922035]
36. Kaluza D, Kroll J, Gesierich S, Yao TP, Boon RA, Hergenreider E, Tjwa M, Rössig L, Seto E, Augustin HG, et al. Class IIb HDAC6 regulates endothelial cell migration and angiogenesis by deacetylation of cortactin. EMBO J. 2011;30:4142–4156. [PubMed: 21847094]
37. Janjanam J, Rao GN. Novel role of cortactin in G protein-coupled receptor agonist-induced nuclear export and degradation of p21Cip1. Sci Rep. 2016;6:28687. [PubMed: 27363897]
38. Schnoor M, Lai FP, Zarbock A, Kläver R, Polaschegg C, Schulte D, Weich HA, Oelkers JM, Rottner K, Vestweber D. Cortactin deficiency is associated with reduced neutrophil recruitment but increased vascular permeability in vivo. J Exp Med. 2011;208:1721–1735. [PubMed: 21788407]
39. Collin GB, Won J, Hicks WL, Cook SA, Nishina PM, Naggert JK. Meckelin is necessary for photoreceptor intraciliary transport and outer segment morphogenesis. Invest Ophthalmol Vis Sci. 2012;53:967–974. [PubMed: 22247471]

40. Mattapallil MJ, Wawrousek EF, Chan CC, Zhao H, Roychoudhury J, Ferguson TA, Caspi RR. The Rd8 mutation of the Crb1 gene is present in vendor lines of C57BL/6N mice and embryonic stem cells and confounds ocular induced mutant phenotypes. Invest Ophthalmol Vis Sci. 2012;53:2921–2927. [PubMed: 22447858]
41. Mair DB, Elmasli C, Kim JH, Barreto AD, Ding S, Gu L, Weinberg SH, Kim T, Kim DH, Li R. The Arp2/3 complex enhances cell migration on elastic substrates. Mol Biol Cell. 2023;34:ar67. [PubMed: 36989030]
42. Singh NK, Kotla S, Dyukova E, Traylor JG Jr, Orr AW, Chernoff J, Marion TN, Rao GN. Disruption of p21-activated kinase 1 gene diminishes atherosclerosis in apolipoprotein E-deficient mice. Nat Commun. 2015;6:7450. [PubMed: 26104863]
43. Kumar R, Mani AM, Singh NK, Rao GN. PKCθ-JunB axis via upregulation of VEGFR3 expression mediates hypoxia-induced pathological retinal neovascularization. Cell Death Dis. 2020;11:325. [PubMed: 32382040]
44. Kumar R, Janjanam J, Singh NK, Rao GN. A new role for cofilin in retinal neovascularization. J Cell Sci. 2016;129:1234–1249. [PubMed: 26857814]
45. Mani AM, Chattopadhyay R, Singh NK, Rao GN. Cholesterol crystals increase vascular permeability by inactivating SHP2 and disrupting adherens junctions. Free Radic Biol Med. 2018;123:72–84. [PubMed: 29782988]
46. Smith LE, Wesolowski E, McLellan A, Kostyk SK, D'Amato R, Sullivan R, D'Amore PA. Oxygen-induced retinopathy in the mouse. Invest Ophthalmol Vis Sci. 1994;35:101–111. [PubMed: 7507904]
47. Connor KM, Krah NM, Dennison RJ, Aderman CM, Chen J, Guerin KI, Sapieha P, Stahl A, Willett KL, Smith LE. Quantification of oxygen-induced retinopathy in the mouse: a model of vessel loss, vessel regrowth and pathological angiogenesis. Nat Protoc. 2009;4:1565–1573. [PubMed: 19816419]
48. Vähätupa M, Prince S, Vataja S, Mertimo T, Kataja M, Kinnunen K, Marjomäki V, Uusitalo H, Komatsu M, Järvinen TA, et al. Lack of R-Ras Leads to Increased Vascular Permeability in Ischemic Retinopathy. Invest Ophthalmol Vis Sci. 2016;57:4898–4909. [PubMed: 27654416]
49. Xu Q, Qaum T, Adamis AP. Sensitive blood-retinal barrier breakdown quantitation using Evans blue. Invest Ophthalmol Vis Sci. 2001;42:789–794. [PubMed: 11222542]
50. Brash JT, Ruhrberg C, Fantin A. Evaluating Vascular Hyperpermeability-inducing Agents in the Skin with the Miles Assay. J Vis Exp. 2018;136:57524.
51. Schnoor M, Stradal TE and Rottner K. Cortactin: Cell Functions of A Multifaceted Actin-Binding Protein. Trends Cell Biol. 2018;28:79–98. [PubMed: 29162307]
52. Vogel V, Sheetz M. Local force and geometry sensing regulate cell functions. Nat Rev Mol Cell Biol. 2006;7:265–275. [PubMed: 16607289]
53. Zipfel PA, Bunnell SC, Witherow DS, Gu JJ, Chislock EM, Ring C, Pendergast AM. Role for the Abi/wave protein complex in T cell receptor-mediated proliferation and cytoskeletal remodeling. Curr Biol. 2006;16:35–46. [PubMed: 16401422]
54. Denker SP, Barber DL. Cell migration requires both ion translocation and cytoskeletal anchoring by the Na-H exchanger NHE1. J Cell Biol. 2002;159:1087–1096. [PubMed: 12486114]
55. Wang S, Li X, Parra M, Verdin E, Bassel-Duby R, Olson EN. Control of endothelial cell proliferation and migration by VEGF signaling to histone deacetylase 7. Proc Natl Acad Sci U S A. 2008;105:7738–7743. [PubMed: 18509061]
56. Lamalice L, Le Boeuf F, Huot J. Endothelial cell migration during angiogenesis. Circ Res. 2007;100:782–794. [PubMed: 17395884]
57. Ochoa D, Jarnuczak AF, Viéitez C, Gehre M, Soucheray M, Mateus A, Kleefeldt AA, Hill A, Garcia-Alonso L, Stein F, et al. The functional landscape of the human phosphoproteome. Nat Biotechnol. 2020;38:365–373. [PubMed: 31819260]
58. Høye AM, Couchman JR, Wewer UM, Yoneda A. The Phosphorylation and Distribution of Cortactin Downstream of Integrin α9β1 Affects Cancer Cell Behaviour. Sci Rep. 2016;6:28529. [PubMed: 27339664]
59. Weaver AM, Heuser JE, Karginov AV, Lee WL, Parsons JT, Cooper JA. Interaction of cortactin and N-WASp with Arp2/3 complex. Curr Biol. 2002;12:1270–1278. [PubMed: 12176354]

60. Yang Q, Zhang XF, Pollard TD, Forscher P. Arp2/3 complex-dependent actin networks constrain myosin II function in driving retrograde actin flow. J Cell Biol. 2012;197:939–956. [PubMed: 22711700]
61. Kumar R, Rao GN. Novel Role of Prereplication Complex Component Cell Division Cycle 6 in Retinal Neovascularization. Arterioscler Thromb Vasc Biol. 2022;42:407–427. [PubMed: 35236105]
62. Yan Z, DeGregori J, Shohet R, Leone G, Stillman B, Nevins JR, Williams RS. Cdc6 is regulated by E2F and is essential for DNA replication in mammalian cells. Proc Natl Acad Sci U S A. 1998;95:3603–3608. [PubMed: 9520412]
63. Ren Y, He Y, Brown S, Zbornik E, Mlodzianoski MJ, Ma D, Huang F, Mattoo S, Suter DM. A single tyrosine phosphorylation site in cortactin is important for filopodia formation in neuronal growth cones. Mol Biol Cell. 2019;30:1817–1833. [PubMed: 31116646]
64. Harris ES, Nelson WJ. VE-cadherin: at the front, center, and sides of endothelial cell organization and function. Curr Opin Cell Biol. 2010;22:651–658. [PubMed: 20708398]
65. Aird WC. Phenotypic heterogeneity of the endothelium: I. Structure, function, and mechanisms. Circ Res. 2007;100:158–173. [PubMed: 17272818]
66. Pober JS, Sessa WC. Evolving functions of endothelial cells in inflammation. Nat Rev Immunol. 2007;7:803–815. [PubMed: 17893694]
67. Mehta D, Malik AB. Signaling mechanisms regulating endothelial permeability. Physiol Rev. 2006;86:279–367. [PubMed: 16371600]
68. Broman MT, Kouklis P, Gao X, Ramchandran R, Neamu RF, Minshall RD, Malik AB. Cdc42 regulates adherens junction stability and endothelial permeability by inducing alpha-catenin interaction with the vascular endothelial cadherin complex. Circ Res. 2006;98:73–80. [PubMed: 16322481]
69. Kundumani-Sridharan V, Dyukova E, Hansen DE 3rd, Rao GN. 12/15-Lipoxygenase mediates high-fat diet-induced endothelial tight junction disruption and monocyte transmigration: a new role for 15(S)-hydroxyeicosatetraenoic acid in endothelial cell dysfunction. J Biol Chem. 2013;288:15830–15842. [PubMed: 23589307]
70. Yamamoto M, Ramirez SH, Sato S, Kiyota T, Cerny RL, Kaibuchi K, Persidsky Y, Ikezu T. Phosphorylation of claudin-5 and occludin by rho kinase in brain endothelial cells. Am J Pathol. 2008;172:521–533. [PubMed: 18187566]
71. Andriopoulou P, Navarro P, Zanetti A, Lampugnani MG, Dejana E. Histamine induces tyrosine phosphorylation of endothelial cell-to-cell adherens junctions. Arterioscler Thromb Vasc Biol. 1999;19:2286–2297. [PubMed: 10521356]
72. Li X, Padhan N, Sjöström EO, Roche FP, Testini C, Honkura N, Sáinz-Jaspeado M, Gordon E, Bentley K, Philippides A, et al. VEGFR2 pY949 signalling regulates adherens junction integrity and metastatic spread. Nat Commun. 2016;7:11017. [PubMed: 27005951]
73. Iliev AI, Djannatian JR, Nau R, Mitchell TJ, Wouters FS. Cholesterol-dependent actin remodeling via RhoA and Rac1 activation by the Streptococcus pneumoniae toxin pneumolysin. Proc Natl Acad Sci U S A. 2007;104:2897–2902. [PubMed: 17301241]
74. Nohata N, Uchida Y, Stratman AN, Adams RH, Zheng Y, Weinstein BM, Mukouyama YS, Gutkind JS. Temporal-specific roles of Rac1 during vascular development and retinal angiogenesis. Dev Biol. 2016;411:183–194. [PubMed: 26872874]
75. Purola PKM, Nättinen JE, Ojamo MUI, Koskinen SVP, Rissanen HA, Sainio PRJ, Uusitalo HMT. Prevalence and 11-year incidence of common eye diseases and their relation to health-related quality of life, mental health, and visual impairment. Qual Life Res. 2021;30:2311–2327. [PubMed: 33755897]
76. Taipale J, Mikhailova A, Ojamo M, Nättinen J, Väätäinen S, Gissler M, Koskinen S, Rissanen H, Sainio P, Uusitalo H. Low vision status and declining vision decrease Health-Related Quality of Life: Results from a nationwide 11-year follow-up study. Qual Life Res. 2019;28:3225–3236. [PubMed: 31401749]
77. Mizutani M, Kern TS, Lorenzi M. Accelerated death of retinal microvascular cells in human and experimental diabetic retinopathy. J Clin Invest. 1996;97:2883–2890. [PubMed: 8675702]

78. Suto C, Kitano S, Hori S. Optimal timing of cataract surgery and pan-retinal photocoagulation for diabetic retinopathy. Diabetes Care. 2011;34:e123. [PubMed: 21709289]

79. Sivaprasad S, Prevost AT, Vasconcelos JC, Riddell A, Murphy C, Kelly J, Bainbridge J, Tudor-Edwards R, Hopkins D, Hykin P. CLARITY Study Group. 2017. Clinical efficacy of intravitreal aflibercept versus panretinal photocoagulation for best corrected visual acuity in patients with proliferative diabetic retinopathy at 52 weeks (CLARITY): a multicentre, single-blinded, randomised, controlled, phase 2b, non-inferiority trial. Lancet. 2017;389:2193–2203. [PubMed: 28494920]

80. Oser M, Mader CC, Gil-Henn H, Magalhaes M, Bravo-Cordero JJ, Koleske AJ, Condeelis J. Specific tyrosine phosphorylation sites on cortactin regulate Nck1-dependent actin polymerization in invadopodia. J Cell Sci. 2010;123:3662–3673. [PubMed: 20971703]

81. Doornaert B, Leblond V, Planus E, Galiacy S, Laurent VM, Gras G, Isabey D, Lafuma C. Time course of actin cytoskeleton stiffness and matrix adhesion molecules in human bronchial epithelial cell cultures. Exp Cell Res. 2003;287:199–208. [PubMed: 12837276]

82. Tavares S, Vieira AF, Taubenberger AV, Araújo M, Martins NP, Brás-Pereira C, Polónia A, Herbig M, Barreto C, Otto O, et al. Actin stress fiber organization promotes cell stiffening and proliferation of pre-invasive breast cancer cells. Nat Commun. 2017;8:15237. [PubMed: 28508872]

83. Ziegler ME, Jin YP, Young SH, Rozengurt E, Reed EF. HLA class I-mediated stress fiber formation requires ERK1/2 activation in the absence of an increase in intracellular Ca2+ in human aortic endothelial cells. Am J Physiol Cell Physiol. 2012;303:C872–C882. [PubMed: 22914643]

84. Desmoulière A, Geinoz A, Gabbiani F, Gabbiani G. Transforming growth factor-beta 1 induces alpha-smooth muscle actin expression in granulation tissue myofibroblasts and in quiescent and growing cultured fibroblasts. J Cell Biol. 1993;122:103–111. [PubMed: 8314838]

85. Gerhardt H, Golding M, Fruttiger M, Ruhrberg C, Lundkvist A, Abramsson A, Jeltsch M, Mitchell C, Alitalo K, Shima D, et al. VEGF guides angiogenic sprouting utilizing endothelial tip cell filopodia. J Cell Biol. 2003;161:1163–1177. [PubMed: 12810700]

86. Hoelzle MK, Svitkina T. The cytoskeletal mechanisms of cell-cell junction formation in endothelial cells. Mol Biol Cell. 2012;23:310–323. [PubMed: 22090347]

87. Helwani FM, Kovacs EM, Paterson AD, Verma S, Ali RG, Fanning AS, Weed SA, Yap AS. Cortactin is necessary for E-cadherin-mediated contact formation and actin reorganization. J Cell Biol. 2004;164:899–910. [PubMed: 15024035]

88. Ninchoji T, Love DT, Smith RO, Hedlund M, Vestweber D, Sessa WC, Claesson-Welsh L. eNOS-induced vascular barrier disruption in retinopathy by c-Src activation and tyrosine phosphorylation of VE-cadherin. Elife. 2021;10:e64944. [PubMed: 33908348]

89. Tehrani S, Tomasevic N, Weed S, Sakowicz R, Cooper JA. Src phosphorylation of cortactin enhances actin assembly. Proc Natl Acad Sci U S A. 2007;104:11933–11938. [PubMed: 17606906]

90. Martini V, Gattazzo C, Frezzato F, Trimarco V, Pizzi M, Chiodin G, Severin F, Scomazzon E, Guzzardo V, Saraggi D, et al. Cortactin, a Lyn substrate, is a checkpoint molecule at the intersection of BCR and CXCR4 signalling pathway in chronic lymphocytic leukaemia cells. Br J Haematol. 2017;178:81–93. [PubMed: 28419476]

91. Yu Y, Suryo Rahmanto Y, Lee MH, Wu PH, Phillip JM, Huang CH, Vitolo MI, Gaillard S, Martin SS, Wirtz D, et al. Inhibition of ovarian tumor cell invasiveness by targeting SYK in the tyrosine kinase signaling pathway. Oncogene. 2018;37:3778–3789. [PubMed: 29643476]

92. Zhang X, Shrikhande U, Alicie BM, Zhou Q, Geahlen RL. Role of the protein tyrosine kinase Syk in regulating cell-cell adhesion and motility in breast cancer cells. Mol Cancer Res. 2009;7:634–644. [PubMed: 19435818]

HIGHLIGHTS

- VEGFA phosphorylates cortactin at Y421, Y453, and Y470 residues in ECs.
- Cortactin phosphorylation at Y470 residue is required for its interaction with Arp2/3 and CDC6 in enhancing actin polymerization and DNA synthesis, respectively, in promoting the angiogenic responses of ECs.
- Cortactin phosphorylation at Y421 residue leads to disruption of its interaction with VE-cadherin and AJs, resulting in vascular leakage.
- Whereas Lyn activation is required for cortactin phosphorylation at Y470 residue mediating retinal neovascularization, activation of Syk is needed for cortactin phosphorylation at Y421 residue in the modulation of vascular leakage.

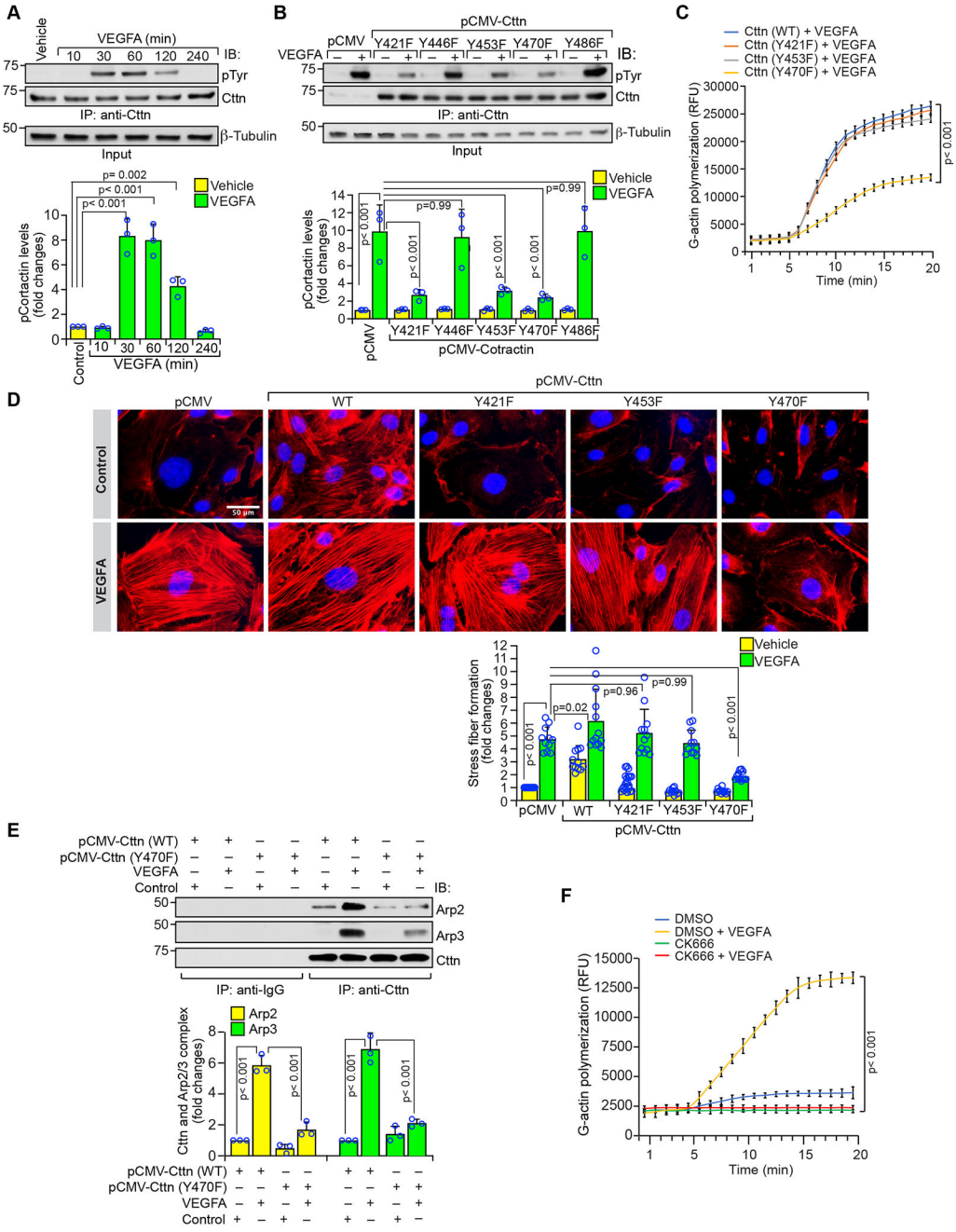

Figure 1: VEGFA-induced actin polymerization requires cortactin phosphorylation at Y470 residue.

A. Quiescent HRMVECs were treated with vehicle or VEGFA (40 ng/ml) for the indicated time points, and equal amounts of protein from control and each treatment were immunoprecipitated with anti-cortactin antibody, followed by analysis of immunocomplexes by WB using pTyr antibody. The blot was normalized for cortactin total protein. B. HRMVECs that were transfected with empty vector or the indicated Cttn phospho Tyr mutant vector were synchronized, treated with vehicle or VEGFA for 30 min, and equal amounts of protein from control and each treatment immunoprecipitated with anti-cortactin

antibody. The immunocomplexes were analyzed by WB using pTyr antibody, and the blot was normalized for cortactin. The Input proteins in both panels A and B were analyzed by WB for β-tubulin. C. HRMVECs were transfected with pCMV Cttn-WT, or pCMV Cttn-Y421F or pCMV Cttn-Y453F or pCMV Cttn-Y470F expression vectors, quiesced, treated with VEGFA for 30 min, followed by preparation of respective cell extracts. The cell extracts containing equal amounts of protein from each regimen were immunoprecipitated with anti-cortactin antibody, and the immunocomplexes subjected to actin polymerization assay as described in Materials and Methods. D. HRMVECs were transfected with pCMV or pCMV Cttn-WT, or pCMV Cttn-Y421F or pCMV Cttn-Y453F or pCMV Cttn-Y470F expression vectors, quiesced, treated with vehicle or VEGFA for 2 h and stained with Phalloidin (scale bar, 50 μm). E. HRMVECs were transfected with pCMV Cttn-WT or pCMV Cttn-Y470F expression vectors, quiesced, treated with and without VEGFA for 30 min, and cell extracts prepared. Equal amounts of protein from control and VEGFA-treatment were immunoprecipitated with anti-cortactin antibody, and the immunocomplexes analyzed by WB for the indicated proteins using their specific antibodies. F. Quiescent HRMVECs were treated with and without VEGFA for 30 min and cell extracts were prepared. Equal amounts of protein from control and VEGFA treatment were immunoprecipitated with anti-cortactin antibody, and the immunocomplexes subjected to an actin polymerization assay in the presence or absence of Arp2/3 inhibitor, CK666 (50 μM). The bar graphs represent quantitative analyses of three biological replicates and the values are presented as Mean ± SD. The data were analyzed by 1-way ANOVA and the statistical significance was represented by p. In Figure 1C and 1F, the values at the end time points were used to determine the p values.

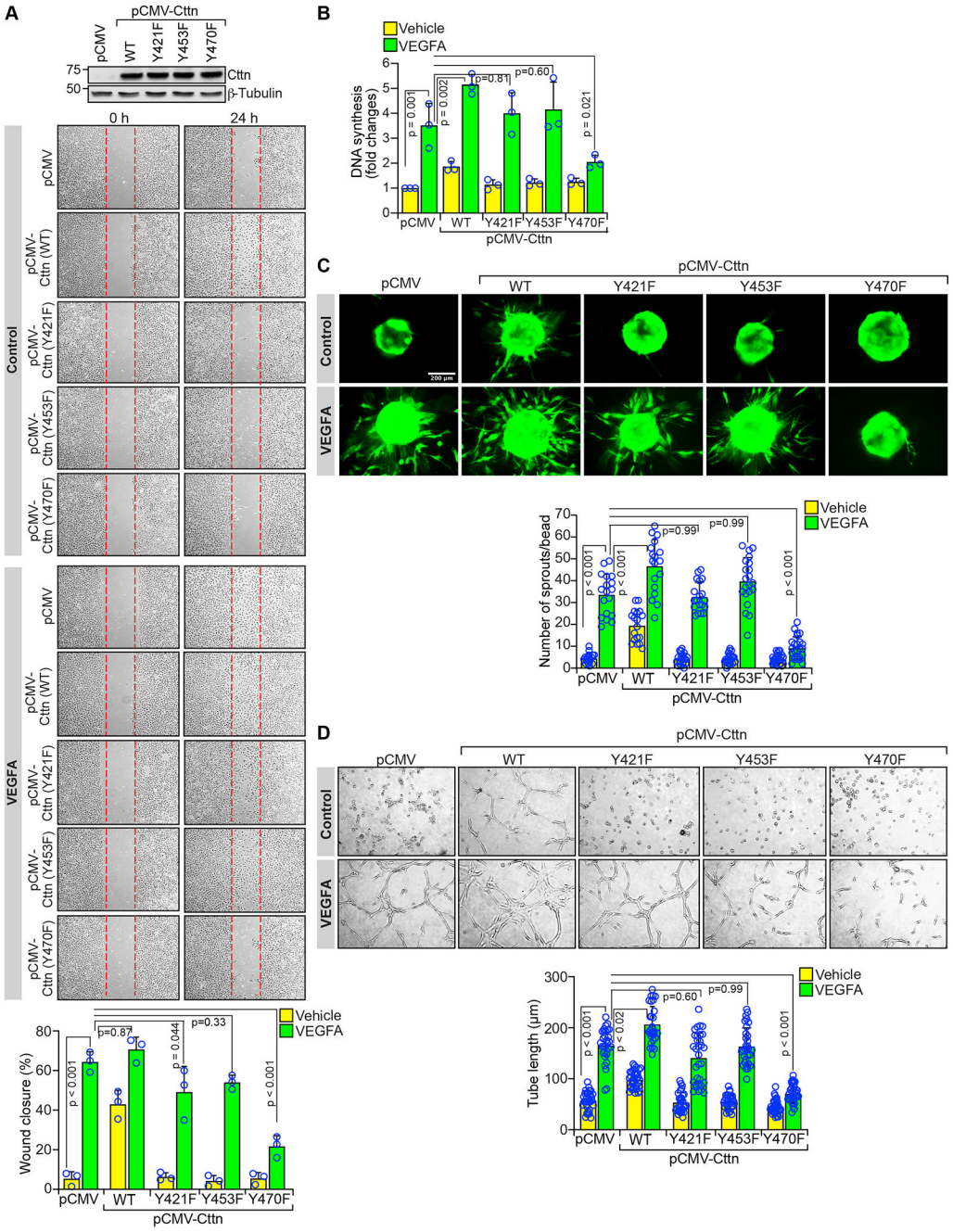

Figure 2: VEGFA-induced HRMVEC migration, proliferation, sprouting and tube formation require cortactin phosphorylation at Y470 residue.

A. HRMVECs that were transfected with empty vector or the indicated cortactin expression vector were synchronized and subjected to VEGFA-induced migration (A), proliferation (B), sprouting (C), or tube formation (D) assays. Bar graphs represent quantitative analyses, and the values are presented as means ± SD. The scale bar in panel C is 200 μm. The scale for panels A and D is 1 mm from the extreme left to the extreme right for each image. The WB analysis in the bottom of panel A shows overexpression of WT and the indicated phospho Tyr mutant of cortactin in HRMVECs. The bar graphs represent quantitative analyses of

three biological replicates and the values are presented as Mean ± SD. The data were analyzed by 1-way ANOVA and the statistical significance was represented by p.

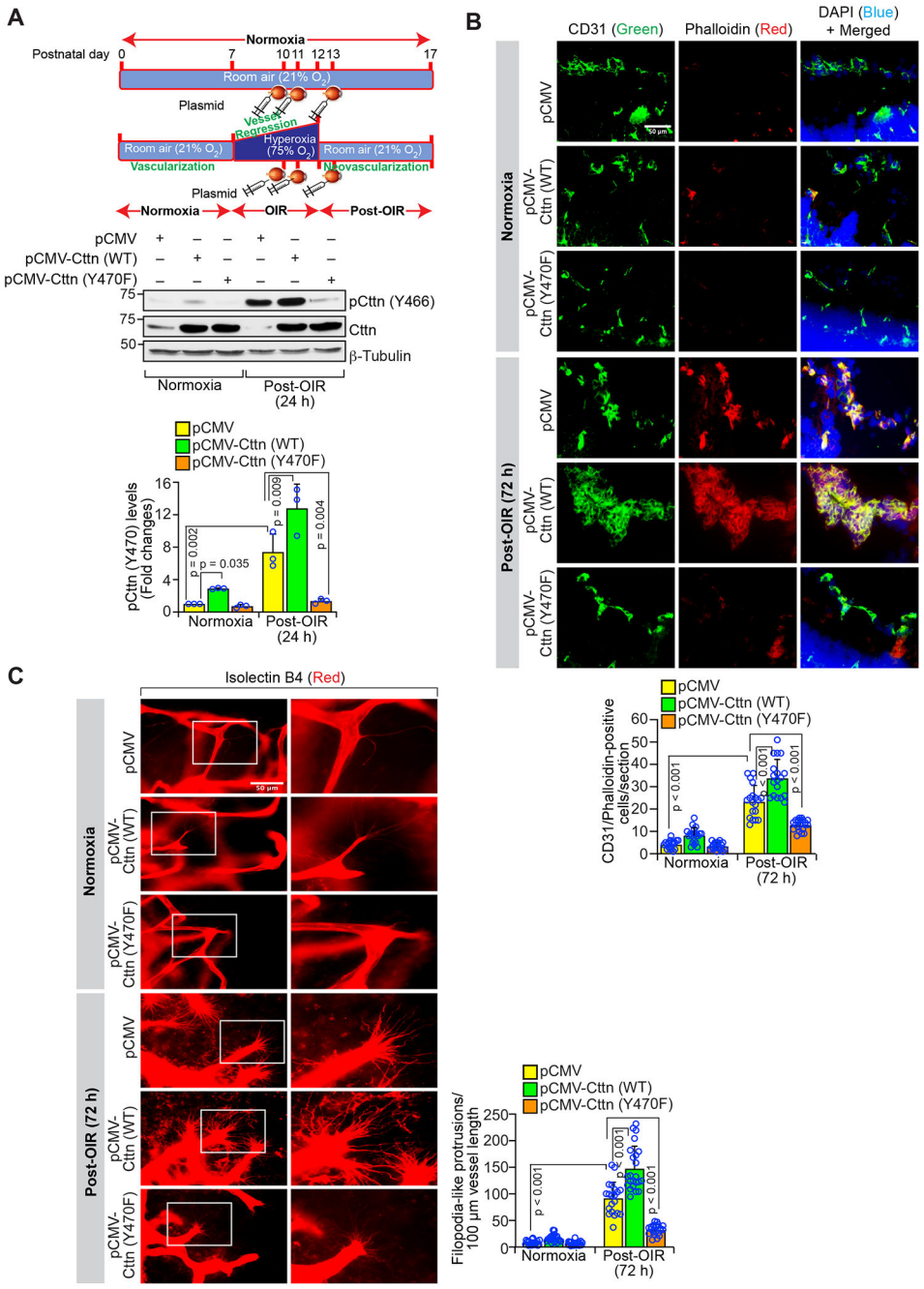

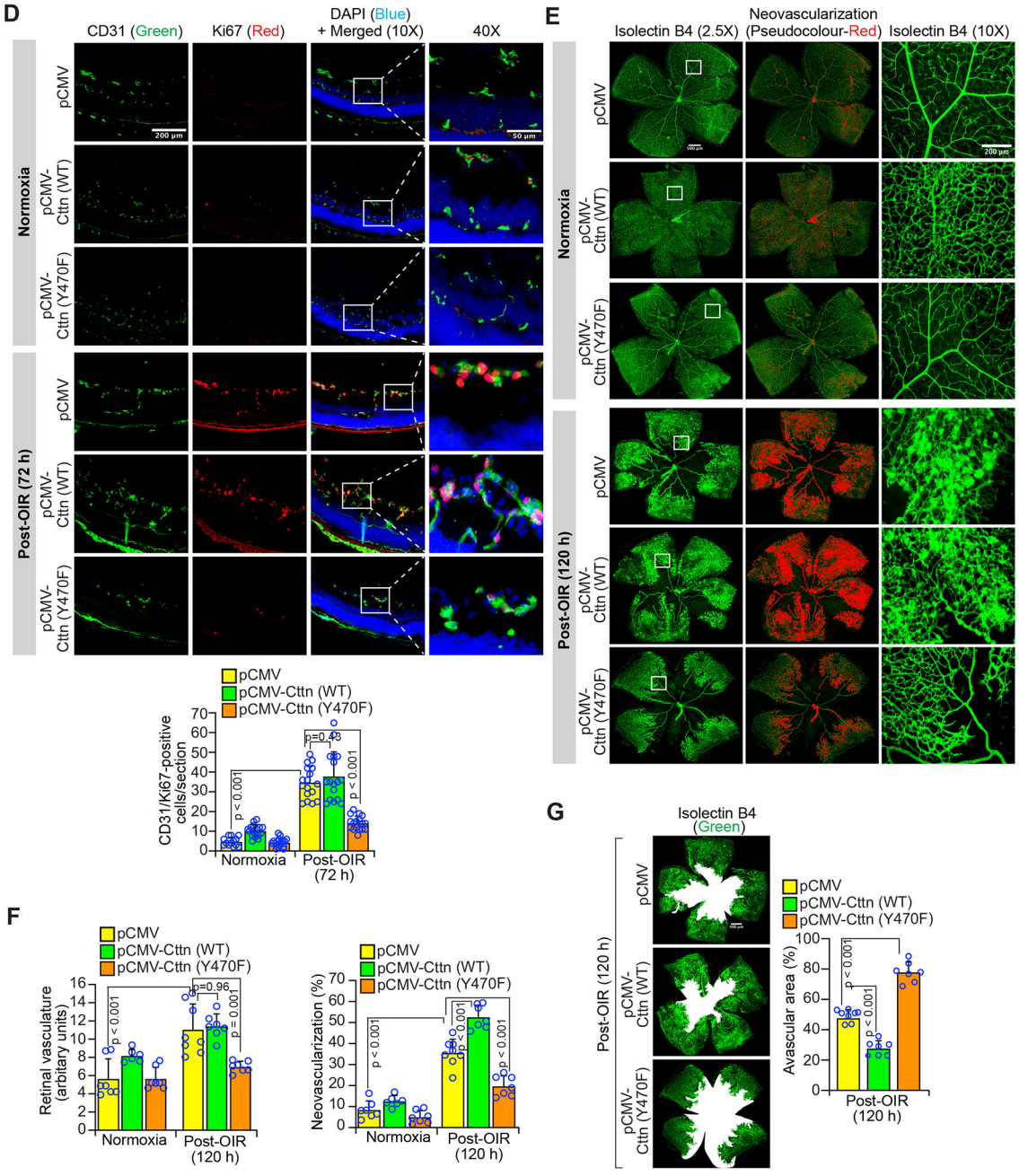

Figure 3: OIR-induced retinal neovascularization requires cortactin phosphorylation at Y470 residue.

A. Upper panel: Schematic diagram of oxygen-induced retinopathy (OIR) induction and the time of intravitreal injections of plasmid DNAs into mouse pups. Lower panel: WT mouse pups with dams were housed in normoxia or in a hyperoxia chamber (75% O_2) from P7 to P12. At P10 and P11, the normoxic and hyperoxic mouse pups were intravitreally injected with pCMV or pCMV-Cttn (WT) or pCMV-Cttn (Y470F) plasmid DNA (1 µg/0.5 µl/eye/ injection) and the eyes from normoxic and 24-h of post-OIR pups (P13) were enucleated and retinal extracts prepared. Equal amounts of protein from retinal extracts were analyzed

by WB for Cttn Y466 phosphorylation using its phospho-specific antibody, and blot was reprobed for total cortactin and β-tubulin. B. Normoxic and hyperoxic mouse pups were injected intravitreally with 1 μg/0.5 μl/eye/injection of pCMV or pCMV-Cttn (WT) or pCMV-Cttn (Y470F) plasmid DNA at P10, P11 and P13 and at 72-h of post-OIR (P15), the eyes then enucleated, fixed, subjected to cross sections, and stained for CD31 along with Phalloidin (scale bar, 50 μm). C. All the conditions were the same as in panel B except that at 72-h of post-OIR (P15), the eyes were enucleated, fixed, retinas isolated, stained with isolectin B4, flat mounts made and examined for filopodia-like protrusions formation at 40X magnification (scale bar, 50 μm). D. All the conditions were the same as in panel B except that the retinal cross sections were coimmunostained for CD31 and Ki67. Retinal EC proliferation was measured by counting CD31 and Ki67-positive cells that extended anterior to the internal limiting membrane in each section and shown in the bar graph. The scale bars in the far left and far right columns are 200 μm and 50 μm, respectively. E. All the conditions were the same as in panel B except that at 120-h of post-OIR (P17), the eyes were enucleated, fixed, retinas isolated, stained with isolectin B4, and prepared as flat mounts. Retinal vascularization is shown in the first column at 2.5X magnification (scale bar, 500 μm) and neovascularization is highlighted in pseudo red in the second column. The third column shows the selected rectangular areas of the images in the first column at 10X magnification (scale bar, 200 μm). F-G. Retinal vasculature (F, left), retinal neovascularization (F, right panel), and avascular area (G) were determined as described in “Materials and Methods” using the retinal flat mounts that were prepared in panel E. The scale bar in panel G is 500 μm. The OIR experiments in pups were not performed gender-wisely as pups were sexually immature. The bar graphs represent quantitative analyses of at least seven biological replicates and the values are presented as Mean ± SD. The data were analyzed by 1-way ANOVA and the statistical significance was represented by p.

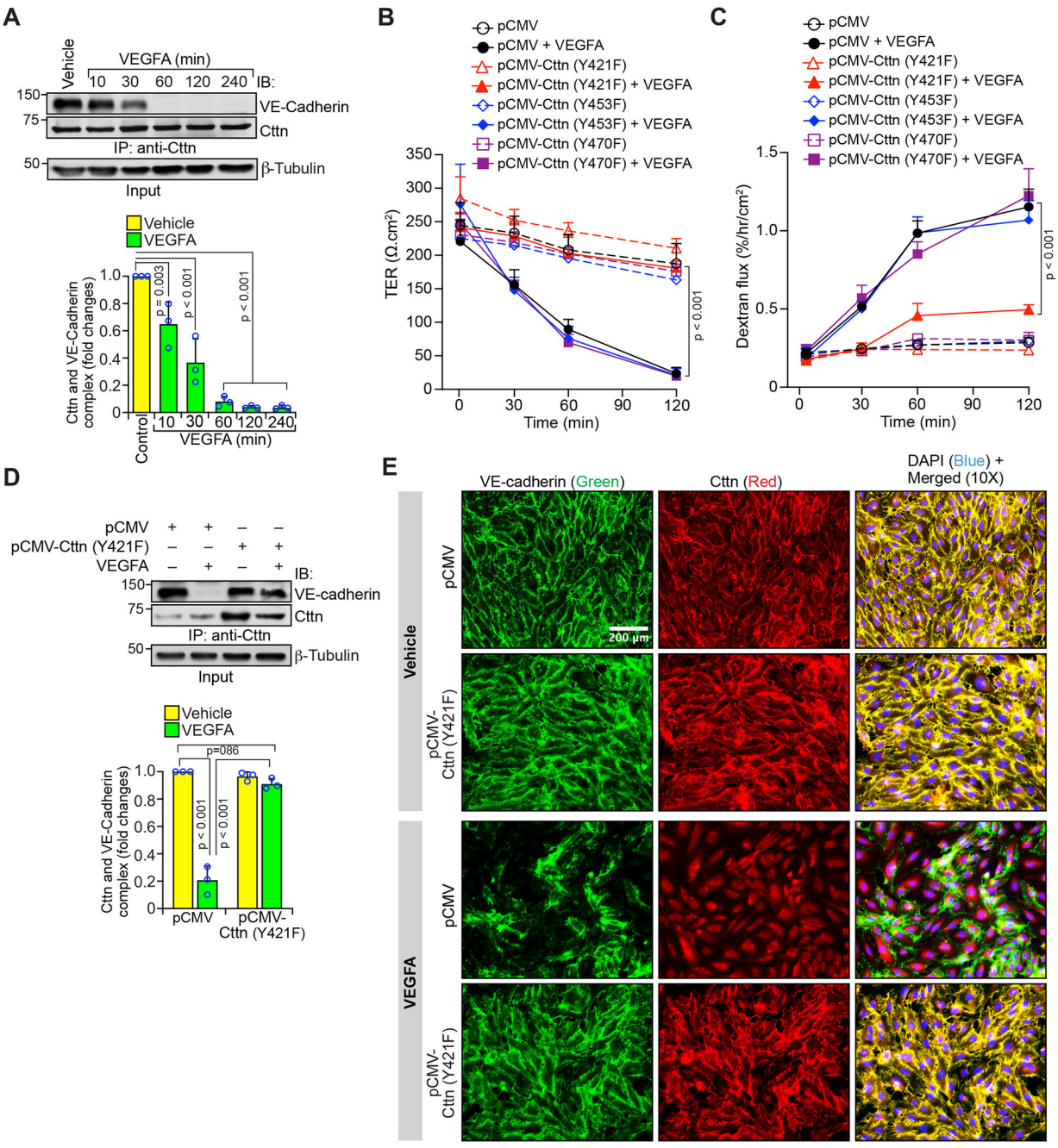

Figure 4: VEGFA-induced AJ disruption requires cortactin phosphorylation at Y421.

A. Quiescent HRMVECs were treated with vehicle or VEGFA (40 ng/ml) for the indicated time points, and equal amounts of protein from each regimen were immunoprecipitated with anti-cortactin antibody. The immunocomplexes were analyzed by WB using VE-cadherin antibody, and the blot was normalized to cortactin. B. HRMVECs that were transfected with empty vector or the indicated Cttn pTyr mutant expression vectors were synchronized, treated with vehicle or VEGFA, followed by measurement of TER as described in "Materials and Methods". C. All the conditions were the same as in panel B except

that dextran flux was measured as described in “Materials and Methods.” D. HRMVECs that were transfected with empty vector or pCMV-Cttn (Y421F) expression vector were synchronized, treated with vehicle or VEGFA, and equal amounts of protein from each regimen immunoprecipitated with anti-cortactin antibody. The immunocomplexes were analyzed by WB using VE-cadherin antibody, and the blot was normalized to cortactin. The input proteins in panels A and D were analyzed by WB for β-tubulin. E. All the conditions were the same as in panel D except that the cells were coimmunostained for VE-cadherin and cortactin (scale bar, 200 μm). The bar graphs represent quantitative analyses of three biological replicates and the values are presented as Mean ± SD. The data were analyzed by 1-way ANOVA and the statistical significance was represented by p. In Figure 4B and 4C, the values at the end time points were used to determine the p values.

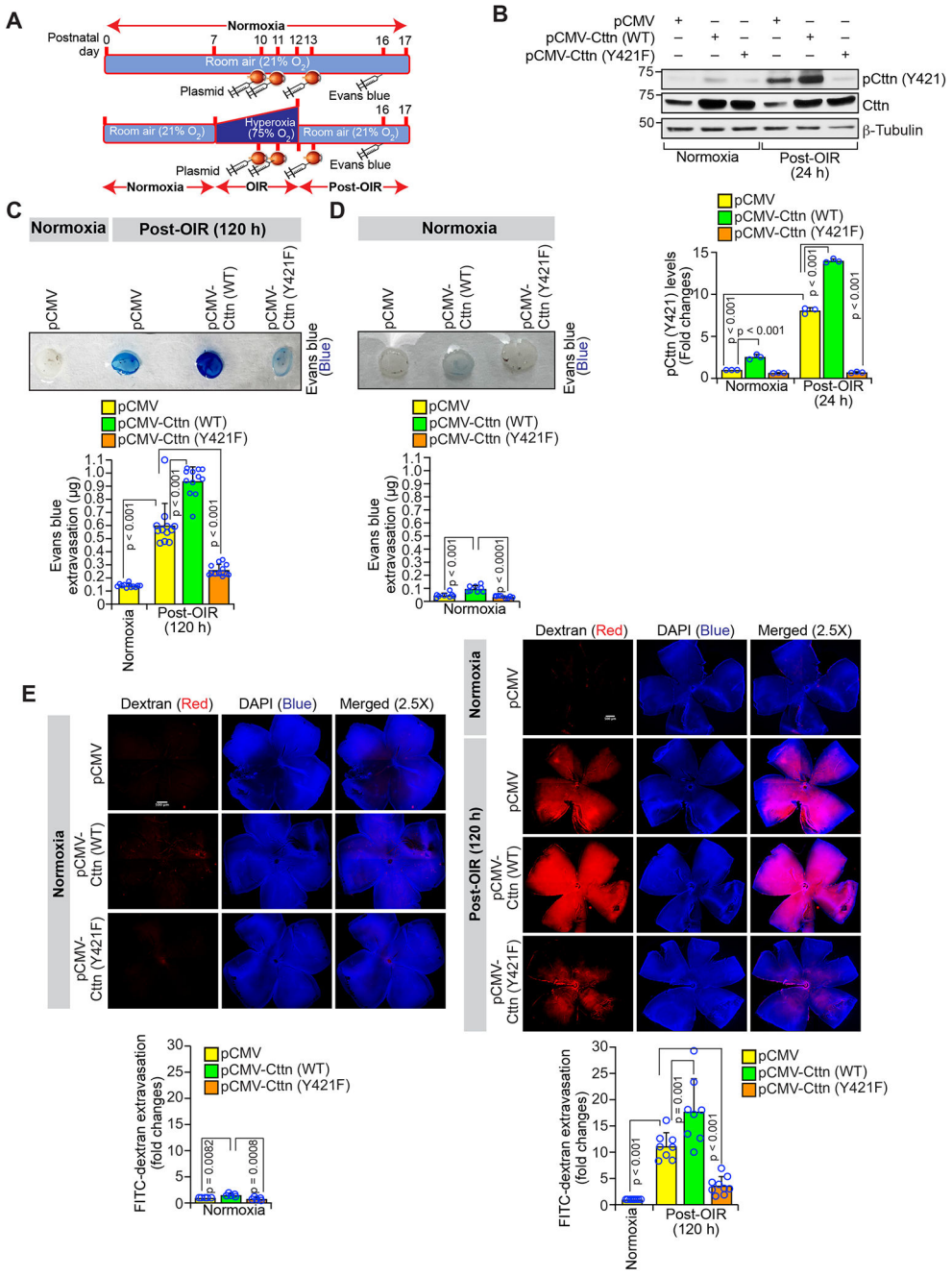

Figure 5: Retinal vascular leakage requires cortactin phosphorylation at Y421 residue.

A. Schematic diagram depicting the time points of intravitreal injections of plasmid DNAs, intraperitoneal injection of EB or intravenous injection of FITC dextran during normoxia and OIR-induction. B. WT mouse pups with dams were housed at normoxia or in a hyperoxia chamber (75% O_2) from P7 to P12. At P10 and P11, the normoxic and hyperoxic mouse pups were intravitreally injected with pCMV or pCMV-Cttn (WT) or pCMV-Cttn (Y421F) plasmid DNA (1 μg/0.5 μl/eye/injection), and the eyes from the normoxic and 24-h of post-OIR pups (P13) were enucleated and retinal extracts prepared. Equal amounts of

protein from the retinal extracts were analyzed by WB for Cttn Y421 phosphorylation using its phospho-specific antibody and the blot was reprobed for total cortactin and β-tubulin. C & D. All the conditions were the same as in panel B except that the P16 normoxic and 96-h of post-OIR (P16) pups were injected intraperitoneally with EB, and 24-h later, the eyes were enucleated, fixed, retinas isolated, and EB extravasation was measured as described in “Materials and Methods.” E. All the conditions were the same as in panel B, except that the P16 normoxic and 96-h of post-OIR pups were injected intravenously with FITC-dextran via tail vein. 24-h later, the eyes were enucleated, fixed, retinas isolated, subjected to flat mount preparation, placed on a coverslip, and examined under a Zeiss inverted fluorescence microscope (Axiovision Observer.z1) to visualize and quantify FITC-dextran in the retinas. The scale bar in panel E is 500 μm. The OIR experiments in pups were not performed gender-wisely as pups were sexually immature. The bar graphs represent quantitative analyses of at least seven biological replicates and the values are presented as Mean ± SD. The data were analyzed by 1-way ANOVA and the statistical significance was represented by p.

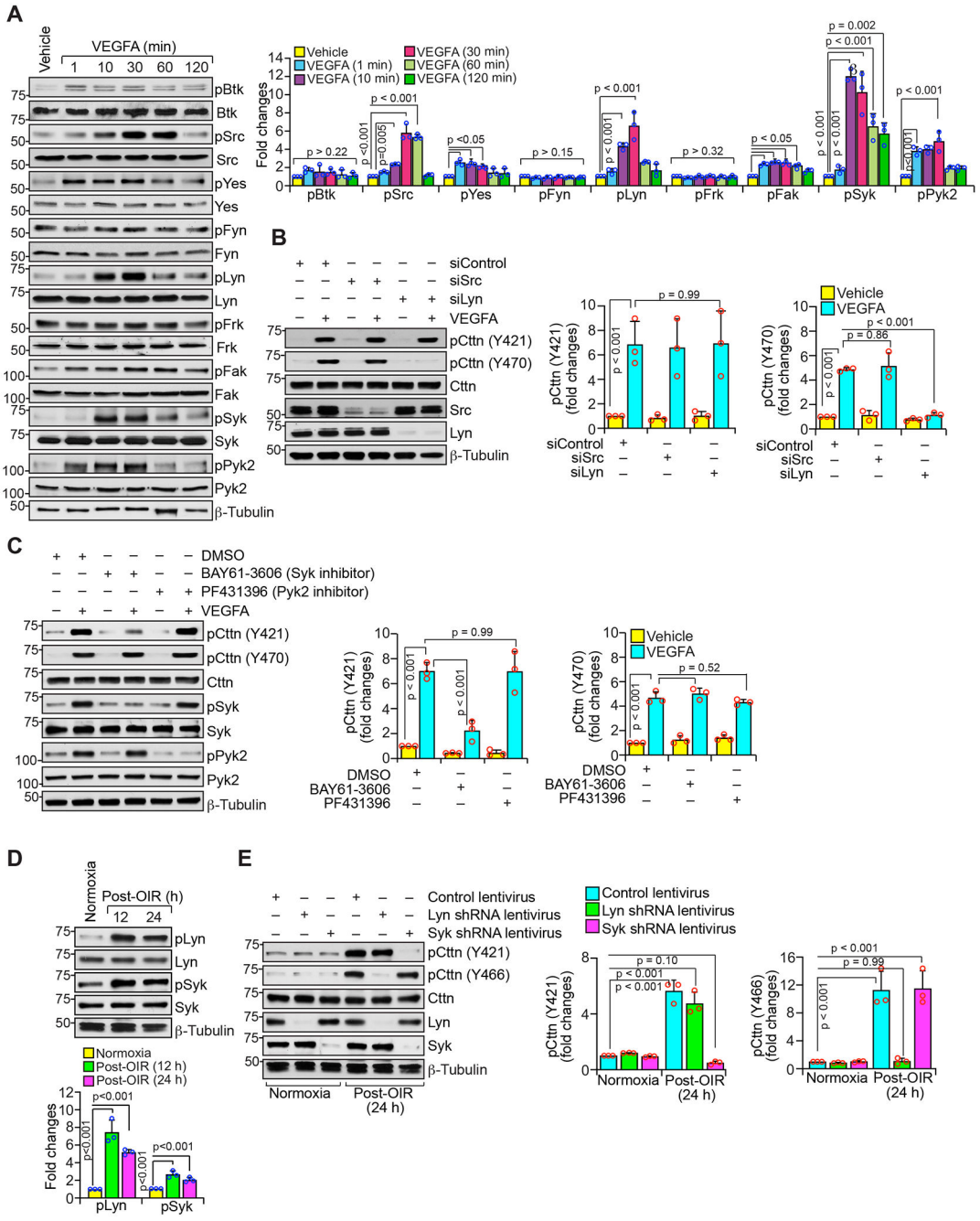

Figure 6: Lyn and Syk mediate VEGFA/OIR-induced cortactin phosphorylation at Y470/Y466 and Y421 residues, respectively.

A. Western blot analysis of control and various time points of VEGFA-treated HRMVECs for the indicated proteins. B. HRMVECs that were transfected with siControl or siSrc or siLyn and synchronized were treated with and without VEGFA for 30 min, and equal amounts of protein from control and each treatment were probed by WB for the indicated proteins. C. Quiescent HRMVECs were treated with vehicle or VEGFA in the presence and absence of BAY61-3606 (Syk inhibitor) or PF431396 (Pyk2 inhibitor) for 30 min, and cell extracts were prepared. Equal amounts of protein from the control and each treatment were

analyzed by WB for the indicated proteins. D. The proteins from normoxic and the indicated time points of post-OIR pups' retinas were analyzed by WB for the indicated proteins using their specific antibodies. E. All the conditions were the same as in panel D except that normoxic and hyperoxic mouse pups were injected intravitreally with 10^6 TU/0.5 μl/eye of control or Lyn or Syk shRNA lentiviral particles at P10. At P13, retinal extracts were prepared and analyzed by WB for the indicated proteins using their specific antibodies. The bar graphs in Figure 6A–C represent quantitative analyses of three biological replicates and the bar graphs in Figure 6D and 6E represent quantitative analyses of pooled retinal extracts from seven biological replicates and the values are presented as Mean ± SD. The data were analyzed by 1-way ANOVA and the statistical significance was represented by p.

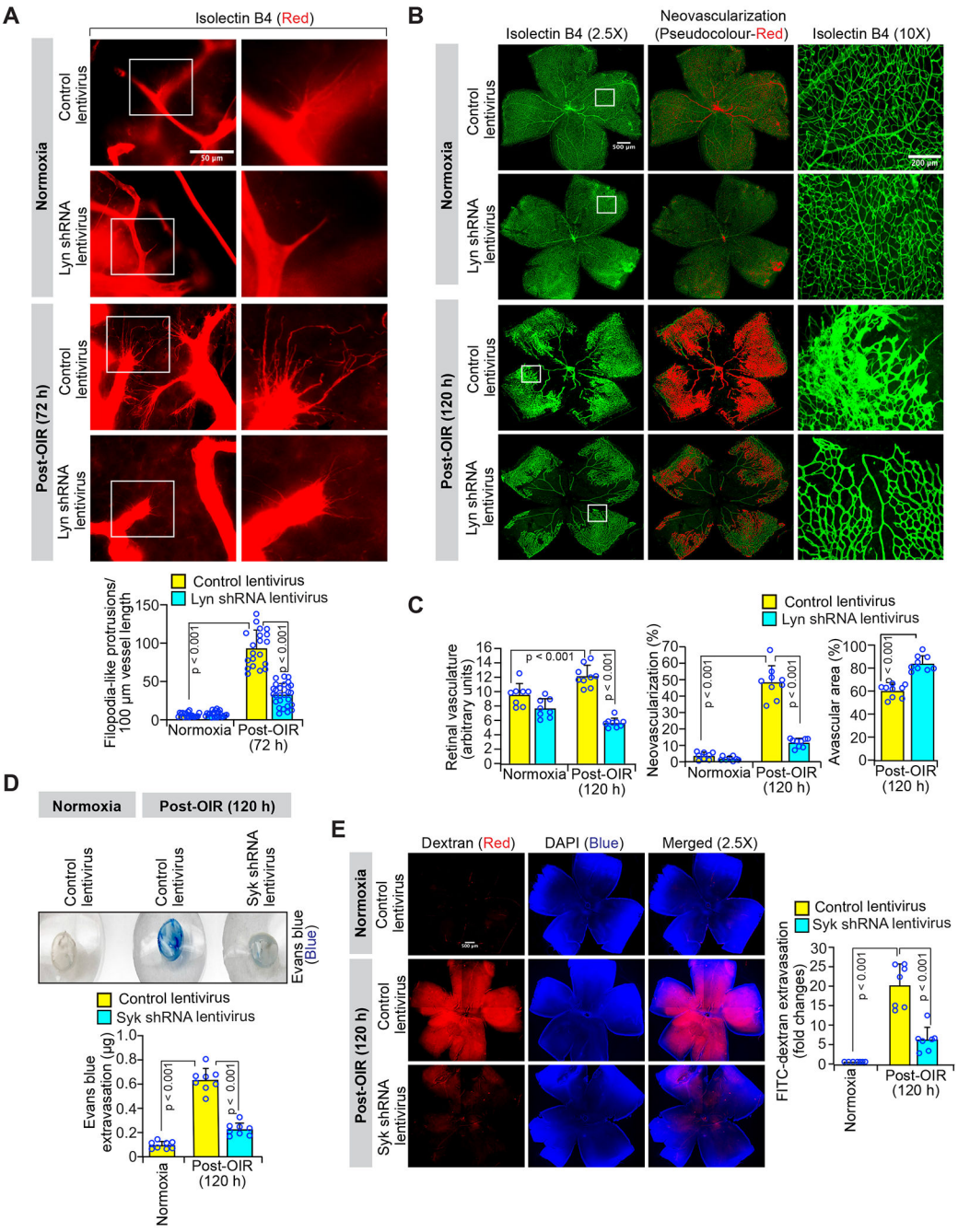

Figure 7: Lyn and Syk mediate OIR-induced retinal neovascularization and vascular leakage, respectively.

A. WT mouse pups with dams were housed in normoxia or in hyperoxia chamber (75% O_2) from P7 to P12. At P10, the normoxic and hyperoxic mouse pups were injected intravitreally with 10^6 TU/0.5 µl/eye of control or Lyn shRNA lentiviral particles, and the eyes from P15 normoxic and 72-h of post-OIR pups (P15) enucleated and fixed. From these, retinas were then isolated, stained with isolectin B4, and subjected to flat mount preparation followed by examination for filopodia-like protrusions at 40X magnification (scale bar, 50 µm). B. All the conditions were the same as in panel A except that, eyes were enucleated, fixed and

subjected to aforementioned protocol at 120-h of post-OIR (P17). Retinal vascularization is shown in the first column at 2.5X magnification (scale bar, 500 μm), and neovascularization is highlighted in pseudocolour (red) in the second column. The third column shows the selected rectangular areas of the images in the first column at 10X magnification (scale bar, 200 μm). C. Retinal vasculature, retinal neovascularization, and avascular area were determined as described in "Materials and Methods" using the retinal flat mounts prepared in panel B. D. All the conditions were the same as in panel A except that at P10, the normoxic and hyperoxic pups were injected intravitreally with 10^6 TU/0.5 μl/eye of control or Syk shRNA lentiviral particles. The normoxic (P16) and 96-h of post-OIR pups were then injected intraperitoneally with EB and 24 h later, the eyes were enucleated, fixed, their retinas isolated, and EB extravasation measured as described in "Materials and Methods." E. All the conditions were the same as in panel D except that the normoxic (P16) and 96-h of post-OIR pups were injected intravenously with FITC-dextran via tail vein. Twenty-four hours later, the eyes were enucleated, fixed, followed by isolation of their retinas, preparation of flat mounts and placing onto a coverslip before final examination with a Zeiss inverted fluorescence microscope (Axiovision Observer.z1), to visualize and quantify FITC-dextran in the retinas. The OIR experiments in pups were not performed gender-wisely as pups were sexually immature. The bar graphs represent quantitative analyses of at least seven biological replicates and the values are presented as Mean ± SD. The data were analyzed by 1-way ANOVA and the statistical significance was represented by p.

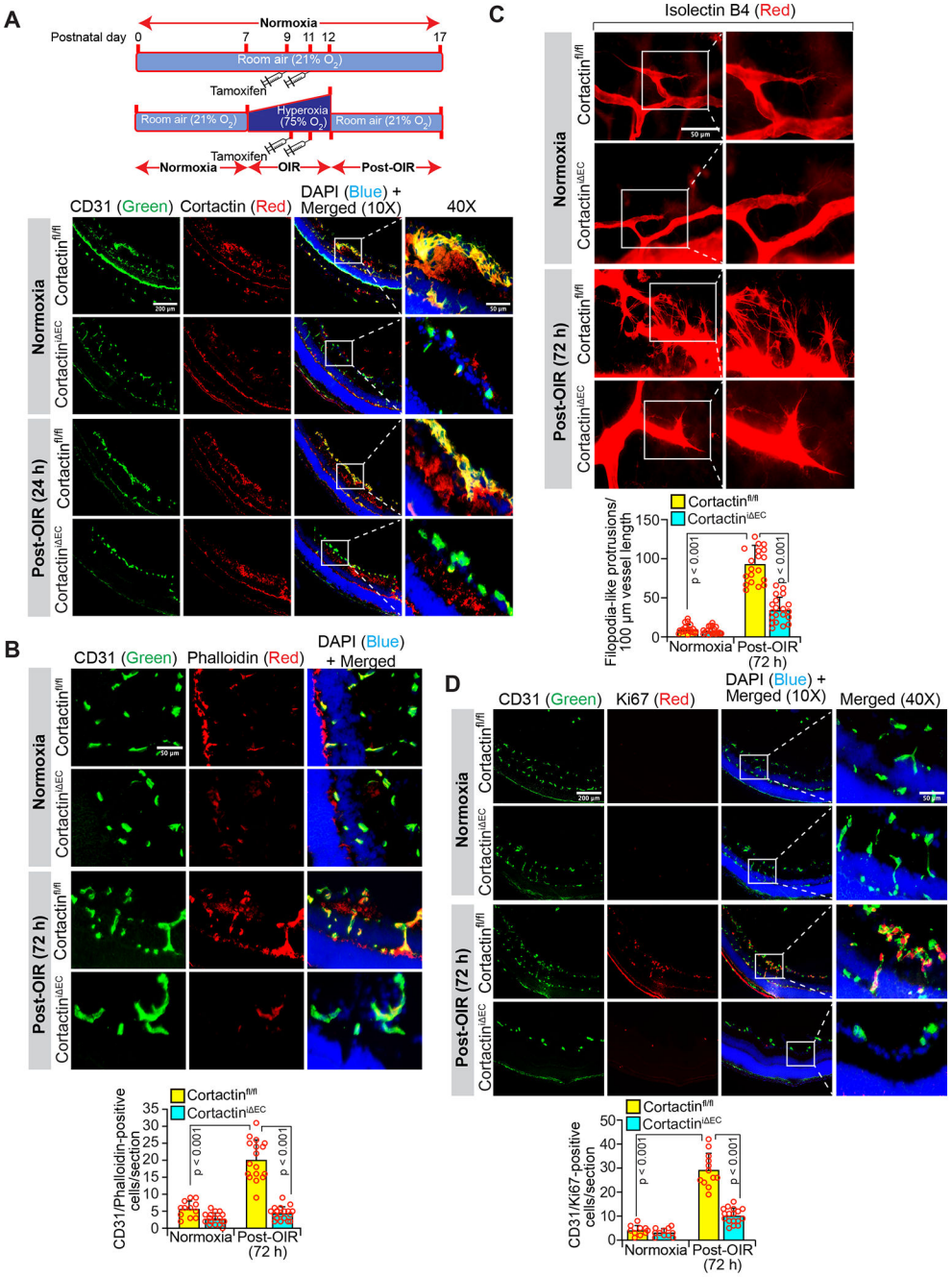

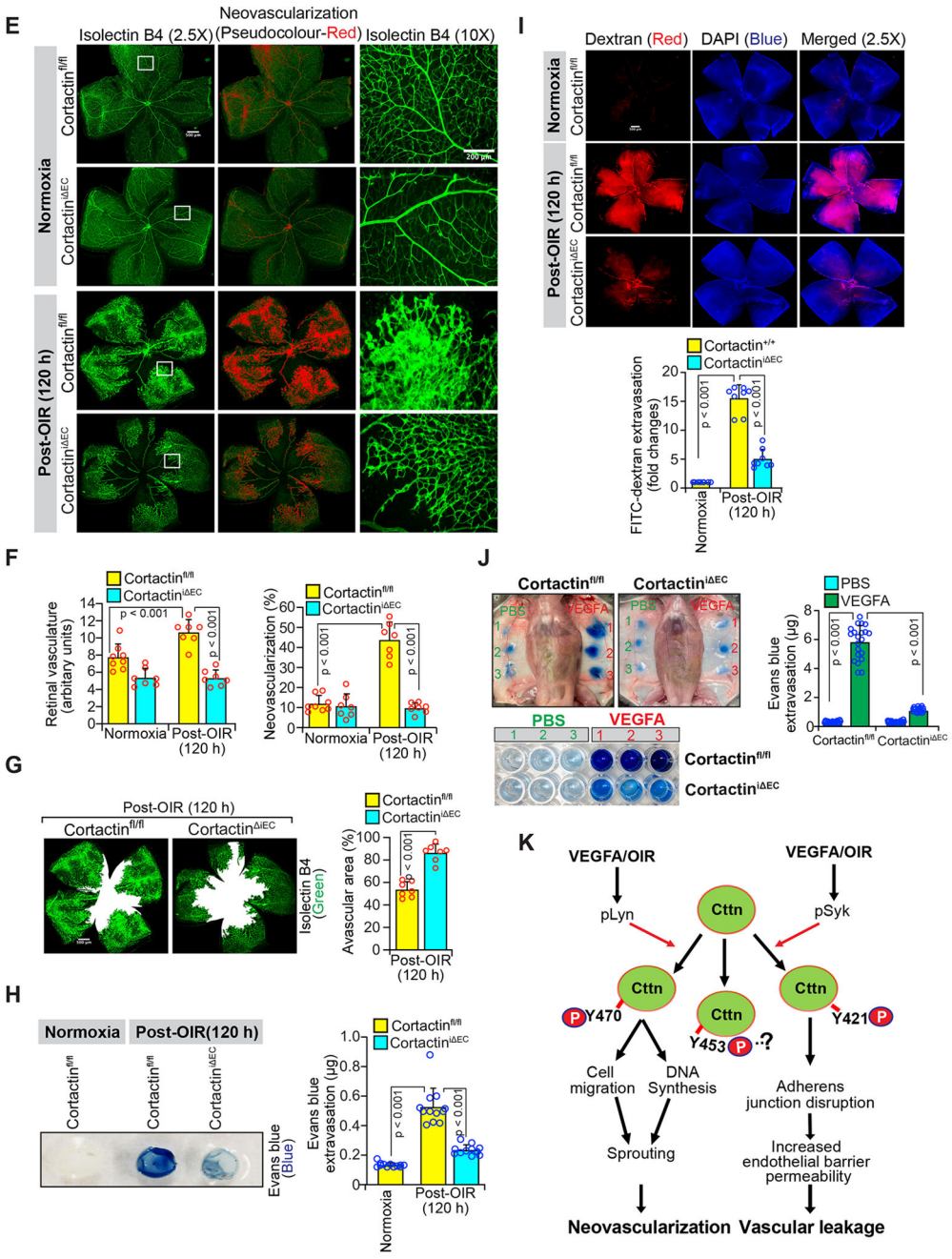

Figure 8: EC-specific conditional deletion of cortactin suppresses OIR-induced retinal neovascularization and vascular leakage.

A. Upper panel: Schematic diagram of Cre activation by tamoxifen both during normoxic and hyperoxic periods in Cortactin$^{flox/flox}$:Cdh5-Cre^{ERT2} mouse pups. Bottom panel: Retinal cross sections from P13 normoxic and 24-h of post-OIR (P13) Cortactin$^{flox/flox}$ and Cortactin$^{i\Delta EC}$ pups were co-immunostained for CD31 and cortactin. The scale bars in the far left and far right columns are 200 μm and 50 μm, respectively. B & D. Retinal cross sections from P15 normoxic and 72-h of post-OIR (P15) Cortactin$^{flox/flox}$ and Cortactin$^{i\Delta EC}$ pups were co-immunostained for CD31 and Phalloidin (B) or CD31 and Ki67 (D). The

scale bar in panel B is 50 μm and the scale bars in panel D are 200 μm (far left column) and 50 μm (far right column), respectively. C. Retinas from P15 normoxic and 72-h of post-OIR (P15) Cortactin$^{flox/flox}$ and Cortactin$^{i\Delta EC}$ pups were stained with isolectin B4, and the flat mounts observed for filopodia-like protrusions in the vascular front at 40X magnification (scale bar, 50 μm). E. Retinas from P17 normoxic and 120-h of post-OIR (P17) Cortactin$^{flox/flox}$ and Cortactin$^{i\Delta EC}$ pups were stained with isolectin B4, the flat mounts observed for neovascularization. Retinal vascularization is shown in the first column at 2.5X magnification (scale bar, 500 μm), and neovascularization is highlighted in pseudo red in the second column. The third column shows the selected rectangular areas of the images in the first column at 10X magnification (scale bar, 200 μm). F-G. Retinal vasculature (F, left), retinal neovascularization (F, right), and avascular area (G) were determined as described in “Materials and Methods” using the retinal flat mounts prepared in panel E. H. The normoxic (P16) and 96-h post-OIR (P16) Cortactin$^{flox/flox}$ and Cortactin$^{i\Delta EC}$ pups were injected intraperitoneally with EB and 24 h later, the eyes were enucleated, fixed, retinas isolated, and EB extravasation measured as described in “Materials and Methods.” I. All the conditions were the same as in panel H except that the pups were injected intravenously with FITC-dextran via tail vein. Twenty-four hours later, the eyes were enucleated, fixed, subjected to retina isolation and flat mount preparation before mounting on a coverslip and examination with a Zeiss inverted fluorescence microscope (Axiovision Observer.z1) to visualize and quantify FITC-dextran in the retinas. J. Cortactin$^{flox/flox}$ and Cortactin$^{i\Delta EC}$ mice were injected intravenously with EB via the tail vein and examined for VEGFA-induced vascular permeability as described in “Materials and Methods.” K. Schematic diagram depicting the role of site-specific Tyr phosphorylation of cortactin in retinal neovascularization and vascular leakage. The OIR experiments in pups were not performed gender-wisely as pups were sexually immature. Regarding Miles’ assay in Figure 8J, which was performed in adult mice, no gender differences were observed as analyzed by Student t test at $p < 0.05$ and therefore the data were combined and presented. The bar graphs represent quantitative analyses of at least seven biological replicates and the values are presented as Mean ± SD. The data in Figure 8A–8F and 8H–8J were analyzed by 1-way ANOVA and the data in Figure 8G were analyzed by Student t test and the statistical significance was represented by p.